SURFACE MORPHOLOGY AND MECHANICAL CHARACTERIZATION OF MoO_3/PEDOT:PSS BLEND THIN FILMS FOR ORGANIC SOLAR CELLS AND LIGHT EMITTING DIODE APPLICATIONS

A Thesis Submitted to the Department of Materials Science and Engineering at

African University of Science and Technology

In Partial Fulfilment of the Requirements for the Degree of

MASTER OF SCIENCE

In The Department of Materials Science and Engineering

BY

KUM TATCHEN BUH

(ID No: 40892)

Abuja, Nigeria

SUPERVISED BY:

DR. VITALIS C. ANYE

SEPTEMBER, 2022

CERTIFICATION

This is to certify that the thesis titled “Surface Morphology and Mechanical Characterization of MoO_3/PEDOT:PSS Blend Thin Films For Organic Solar Cells and Light Emitting Diode Applications” submitted to the school of postgraduate studies, African University of Science and Technology (AUST), Abuja, Nigeria for the award of the Master's degree is a record of original research carried out by Kum Tatchen Buh in the Department of Materials Science and Engineering.

SURFACE MORPHOLOGY AND MECHANICAL CHARACTERIZATION OF MoO_3/PEDOT:PSS BLEND THIN FILMS FOR ORGANIC SOLAR CELLS AND LIGHT EMITTING DIODE APPLICATIONS

By

Kum Tatchen Buh

A THESIS APPROVED BY THE DEPARTMENT OF MATERIALS SCIENCE AND ENGINEERING

RECOMMENDED: _____

Dr. Vitalis C. Anye

(Supervisor)

_____

Dr. Vitalis C. Anye

(Head of Department of Materials Science and Technology)

APPROVED: _____

Chief Academic Officer

ABSTRACT

Access to cheap and reliable electricity is a requirement for improved quality of life and industrialization. Solar energy harvesting for electricity generation has been a promising area where solar cells combined into modules and then panels are used to harvest solar energy for electricity. However, initial acquisition cost of active solar is still a major barrier. There is therefore dire need for efficient and affordable solar technologies to help mitigate current global energy crisis. Organic and perovskite photovoltaics pose superior properties and cheaper cost. Degradation, stability and durability are the current issues faced with organic and perovskite solar cells stopping them from being commercialized or used in a large scale. It is important to carefully study the different thin films layers making up these devices to investigate these issues of stability, degradation and durability. Over the years, both experimental and computational techniques have been used to study these issues. The mechanical properties of these thin film devices are very crucial for development and implementation of mechanical durable devices.

In this work, nanoindentation is mainly employed to investigate the effects of annealing temperatures and MoO_3 blended ratios on the surface morphology, sheet resistance, mechanical properties as well as microstructure of PEDOT:PSS/MoO_3 thin film blends as hole transport materials (HTM) for photovoltaics and OLED applications. Results from this study suggest that, the introduction of different percentages of the transition metal oxide (MoO_3) into PEDOT:PSS significantly modifies the surface morphology, microstructure and mechanical properties in the different temperature regimes. (60 ^{0}C, 80 ^{0}C, 100 ^{0}C, 120 ^{0}C). Furthermore, PEDOT:PSS/MoO_3 thin film blends with small blended ratios of MoO_3 (1:0.1 and 1:0.3) generally exhibit low sheet resistances, better surface morphologies and a good balance in mechanical properties (elastic

modulus and hardness). A balance of properties as in hybrid thin films with low blended ratios is required to develop efficient and mechanical durable electronic devices. Finally, it was also found that, high blended ratios of MoO_3 leads to high surface roughness and high sheet resistance which are unfavorable for device performance.

DEDICATION

To my grandpa, Fan Kum Ezong and grandma, Deborah Sei Kum, I am a product of your great discipline, love and support.

AKNOWLEDGEMENT

Firstly, I would like to thank the Almighty God for His protection, love and guidance throughout my life to date. Without His grace this work would not have been accomplished.

Secondly, my sincere gratitude goes to my supervisor, Dr. Vitalis Anye, for his great support, guidance and impartation during my MSc journey in AUST. I really appreciate your patience and understanding, especially the sleepless nights you had in order to offer me the needed support during my thesis research. Thank you very much Sir! I would also like to thank Dr. Yusuf Afolabi for putting me through the laboratory sessions and his continued support to help me become a better scientist. I would also like to thank Dr. Abdulhakeem Bello for his support and efforts during my stay in AUST. My sincere thanks also goes to Prof. Wole Soboyejor, your introductory lessons into my MSc program gave me more motivation to seek knowledge which can help change the African narrative. To all AUST faculties and technologist, my gratitude for all your efforts and support. I wish to also thank the Principal of Seaside International School, Mrs Agnes Ankrah for her support during my studies.

My sincere gratitude goes to my entire family especially, my mum, Ma Ju and my aunty Dr. Wanai Kum for their continuous support, prayers and for not giving up on me. I appreciate you all!

Finally, a big thank you to my friends, colleagues and the entire MSc 2022 set, I appreciate all the efforts and constructive contributions we provided each other to attain our goals. May God bless you all!

Table of Contents

List of Figures

Figure 4.8: Frequency plots of grid indentation results for as prepared PEDOT:PSS annealed at 60C (a) histogram of hardness with deconvolution results for a bin size of 0.02 GPa, (b) histogram of elastic modulus with deconvolution results for a bin size of 0.5 GPa.

Figure 4.9: Frequency plots of grid indentation results for selected MoO_3/PEDOT:PSS blends (a) histogram of hardness with deconvolution results for a bin size of 0.01 GPa, (b) histogram of elastic modulus with deconvulation results for a bin size of 2 GPa, (c) histogram of elastic modulus, bin size 2 GPa (d) histogram of elastic modulus with deconvulation, bin size 2 GPa.

List of Tables

CHAPTER ONE

1.1 BACKGROUND AND INTRODUCTION

In the past decade, some energy sources have been at the heart of climate change; fossil foils are still chiefly used for energy generation often leading to the release of large amounts of greenhouse gases such as CO_2 and nitrous oxides that have contributed greatly to global warming and drastic climatic changes around the globe. Also, energy crisis and inefficient energy utilization especially in Africa, and energy sustainability issues have become a global concern. Global energy demand and consumption have also increased significantly [1].

In an attempt to combat these adverse climatic concerns from the use of finite fossil foils, much attention has been drawn towards renewable energy sources such as wind and solar as they represent an essential part of the solutions to problems of climate change and pollution, geopolitical risk and energy crisis, price volatility and local or regional economic development. Renewable energy undoubtedly represents a lot of benefits for the present and future generations.

Of all the recent energy sources, solar energy stands as the one with the greatest prospects. Yearly growth rates over the last five years were on average more than 40%, thus making photovoltaic one of the fastest growing industries at present [2], several reasons justify this. Firstly, solar energy produces very little or no polluting by-products and therefore does not add to climate change problems. Also, the endless supply of solar power from the sun in literally all places on earth, makes solar energy the most sustainable and accessible energy source on earth. Furthermore, the use of solar power is an added property value as it helps to save much in energy bills throughout the ownership of the property. Lastly, regardless of what reasons and how fast the oil price and energy prices will increase in the future solar energy will offer a reduction in prices rather than an

increase in the future as there is continuous research on affordable solar power. According to the UN, about 29% of the current energy supply comes from renewable energy sources [3].

These energy challenges have spearheaded research into cleaner, more efficient, and sustainable energy from relatively cheaper organic materials and their hybrids such as perovskites. Energy unavailability is not the only concern, inefficient use of energy for lighting and display is also a major problem. Research into more efficient lighting and display from Organic light emitting devices (OLEDs) is also on the rise due to their superior advantages compared to traditional display and lighting technology; they are thin structures, consume less power, and have high resolution and self-emissive characteristics [4]. OLEDs are expected to in the future replace devices like incandescent lamps and LED displays which are less efficient. Some major progress has been made in the development of perovskites and OLEDs for adoption for energy sustainability. However, most research work on perovskites solar cells (PSCs) still ends at the level of the laboratory even after records of efficiencies of up to 25.2% by 2021 [5], [6] as with the traditional photovoltaics. Research findings show that organic photovoltaics are or will be more cost-effective compared to their traditional counterparts based on inorganic materials such as silicon (Si) wafers and gallium arsenide (Gas). Other key attributes of perovskites over their traditional inorganic counterparts include ease of fabrication, excellent photoelectric properties, ability to achieve high power conversion efficiencies (PCE), lower exciton binding energy, and high optical absorption coefficients (up to 104 cm−1). Secondly, perovskite as the light-absorbing layer can absorb solar energy more efficiently, perovskite materials possess a large dielectric constant and electrons and holes can be effectively transmitted and collected and, electrons and holes can be transmitted simultaneously over distances of 100 nm or more [7]. Despite these benefits, some key challenges of perovskites are; stability of the perovskite layer which degrades on exposure to moisture and

ultraviolet radiations, the toxicity issues with lead which is a major constituent of high-performing hybrid organic/inorganic metal halide PSCs and lastly problems of mechanical durability. Hence, full adoption of perovskite solar cells (PSCs) for large scale synthesis and implementation beyond the lab will need fruitful research in solving these current hurdles faced. More information on the materials is needed for further improvements in performance and stability [8] of the PSCs. Nanoindentation at very low loading conditions has proven to be a suitable technique to investigate more on the mechanical properties of such thin film materials.

Nanoindentation is a 'non-destructive' probing technique used for the investigation and characterization of the mechanical response of materials. Nano scratch on the other hand is a quantitative destructive technique in which critical loads at point(s) of failure are used to compare the cohesive or adhesive properties of thin films, coatings, or bulk materials. This involves a material of known properties having contact with another material whose properties are under investigation. In this technique, an indenter tip with a penetration depth less than 500 nm ISO 14577-1 standards [9] is pressed onto the specimen and the penetration depth is continuously measured. This is a very common and robust technique based on the principles of contact mechanics which is often used to evaluate the mechanical properties of materials through surface measurements. This technique has evolved beyond measurements of just basic design parameters for materials such as hardness and Young's modulus to measurements of other parameters such as creep [10], yield strength [9], [11], and fracture toughness. Nanoindentation is not only limited to experimental measurements, several researchers have carried out nanoindentation and nano scratch simulations based on the finite element analysis (FEA) or finite element method (FEM) with results confirming to experimental results. FEA becomes handy and can give better results for complex stresses and strain field distributions during indentation, especially in cases where there

is difficulty in getting such results experimentally [12]. Numerical analysis as FEA is also important for the back analysis of experimental data in the absence of conventional experimental methods [13].

Thus, as a means to contribute knowledge towards tackling the above problems with OPVs and OLEDs, this project work seeks to use experimental methods to study the surface morphology, electrical characteristics and also by employing nanoindentation and nano scratch to study the hardness, elastic modulus, and frictional resistance of a PEDOT: PSS/MoO_3-ammonia blend hole transport layer for applications in PSCs and OLEDs. This approach is intended to provide more insights on how to re-engineer the devices and improve their mechanical durability and general performance

1.2 AIM AND OBJECTIVES OF THESIS

This research work aims to study the surface morphology, electrical and mechanical properties of solution-processed PEDOT: PSS/MoO_3-ammonia blend hole transport layer for applications in PSCs and OLEDs

The following approach will be employed to achieve these objectives:

- Solutions of the hole transport layers will be prepared and mixed in different compositions,
- These compositions will be spin coated and annealed at different temperatures.
- Nanoindentation will be carried out to get optical images and mechanical properties of the hole transport layer.
- Analysis of data obtained from experiments and calculations of mechanical properties.
- Lastly, indentation data will be analyzed for mechanical properties and inference drawn from this analysis with recommendations for future works.

1.3 PROBLEM STATEMENT

Organic photovoltaics (OPVs) such as perovskites and OLEDs generally exist as a single layer or multilayer thin film structures comprising of an anode, cathode, an active layer, or an emissive layer for a single layer device. In multilayer structures, more layers: a hole transport/injection layer (HTL), and an electron transport layer (ETL) are often added for improved performance. Each of these layers performs specific functions that contribute to the overall functioning of the device. In OPVs such as perovskites, an added hole transport layer (HTL) to a single-layer device is responsible for transporting holes away from the active layer. The materials that make up this layer must have energy levels that match that of the perovskite or OLED, long-term stability in air, and possess intrinsically high hole mobility with good photochemical and thermal stability [14]. This thin film technology is not only common to OPVs and OLEDs but also in other electronic devices, despite these vast areas of application, the mechanical properties of these thin film layers have often been overlooked without thorough investigations. Since such devices operate based on combined functionality from different layers, it is expedient to carefully study the individual layers of such devices, especially the hole transport material making the HTL to fully ascertain their mechanical properties and suitable service conditions as the failure of any layer results in poor performance of the entire device. Therefore, tackling and investigating the mechanical properties of such structures at the nanoscale will help resolve issues of sudden failure and thus aid in the fabrication of more robust and durable devices with improved performances and service life.

1.4 SCOPE AND OUTLINE OF THESIS

In this project work, the scope will be limited to the use of experiments to study the surface morphology, electrical characteristics, and mechanical properties of the PEDOT: PSS/MoO_3-ammonia blend hole transport layer. The focus will be on organic-inorganic thin film layers used

on hybrid solar cells of perovskites and light emitting devices. Also, this work will be limited to the study of properties such as Young's modulus, and hardness using nanoindentation test. The sheet resistance will be measured for different compositions under different annealing conditions and the results analyzed for best performance; these results will be compared to existing data for conformity. Furthermore, morphological analysis of the samples will also aid in drawing inferences and making recommendations for future works.

The thesis begins with a general background and introduction to the research topic in chapter one, chapter two will give a thorough literature review of previous studies on this topic, and chapter three will contain the analytical and experimental methods used for this research. Chapter four will contain the different results from tests and experiments, calculations, and interpretation of the results, and in chapter five inference will be drawn from the results and recommendations made for future work.

CHAPTER TWO

2.1 INTRODUCTION

In this chapter, we look at photovoltaic and OLEDs based on perovskites, their structures, and their working principle. Also, we will discuss organic light emitting devices, their structures, and their working principle. Furthermore, previous works on nanoindentation and FEA of the above device architectures will be discussed.

2.2 PHOTOVOLTAIC TECHNOLOGY AND ITS EMERGENCE

The photovoltaic effect was first discovered by Baquerel in 1839, he observed a photocurrent after platinum electrodes covered with silver halogen were illuminated in an aqueous solution [15].

Fruitful work into photovoltaics started in 1900, Pochettino first observed photoconductivity in the organic material anthracene, photoconductivity in PVK was put in evidence, and the first inorganic photovoltaic cells based on crystalline silicon were developed at Bell laboratories with efficiencies of about 6% [16].

The photovoltaic effect is based on the absorption of photons from solar radiations, excitons are generated and dissociated into charge carriers, and then carriers are collected at electrodes leading to the flow of electrical energy. This effect has been observed in both organic and inorganic materials and their compounds. A similar but opposite effect occurs in OLEDs whereby carriers (holes and electrons) recombine at the emissive layer with light emission.

A major part of the photovoltaic market is controlled by inorganic materials (Si wafers) and their compounds copper indium gallium diselenide (CIGS). This market monopoly is mainly due to peculiar attributes such as high efficiencies, non-toxicity, long lifespan, sustainability, and

availability [17]. However, despite these advantages, the cost of production of crystalline Si solar cells is high and this has given a competitive advantage to thin film Si cells and OPVs devices, also, even higher efficiencies can be achieved at a comparatively low cost in organic materials and their hybrids (perovskites) giving them better prospects for future applications.

Over the years, photovoltaic technology has transitioned from silicon wafers to thin film compounds and at this current stage aimed at very low cost, at optimum efficiencies are organic solar cells and their hybrids (perovskites). This is generally the same case with lighting and display technology, it has transitioned from incandescent lamps to LEDs and now OLEDs which have proven to be more efficient and cost-effective.

Below, perovskites and OLED structures are briefly discussed, their working principles, and major issues faced by these devices.

2.3 PEROVSKITE SOLAR CELLS, STRUCTURES, AND WORKING PRINCIPLE

2.3.1 PEROVSKITE SOLAR CELLS (PSCs)

PSCs have attracted great attention from researchers all over the world and are considered to be one of the top 10 scientific breakthroughs as this novel photovoltaic technology is expected to break the bottleneck of power conversion efficiency at a low cost. The photoelectric power conversion efficiency of the perovskite solar cells has increased from 3.8% in 2009 to 25.2% by 2021 [6], making perovskite solar cells the best potential candidate for the new generation solar cells to replace traditional silicon solar cells in the future.

Perovskites are named after the Russian politician and mineralogist Lev Perovski, the name was originally coined for the mineral calcium titanate($CaTiO_3$) by Gustav Rose [18], and today, 'perovskite' is used to describe ionic compounds with the structural form ABX_3 similar to the crystal structure of $CaTiO_3$ as shown in figure 2.1.

Perovskite materials have attracted wide attention because of the cubic lattice-nested octahedral layered structures and their unique optical, thermal, and electromagnetic properties. Perovskite materials used in solar cells are organic/inorganic metal halide compounds with the perovskite structure, at the vertex of the face-centered cubic lattice is Group A [19] an organic or inorganic cation [20] such as methylammonium(CH3NH3+, MA+), or 3 formamidinium, (CH(NH2)2+, FA+), Group B is the metal cation (Pb2+, Sn2+, Cu2+.) and X is any halogen anion (Cl−, Br−, or I−, or coexistence of several halogens) occupy the core and apex of the octahedra, respectively [8], [20] as shown in figure 2.2. The metal-halogen octahedra are joined together to form a stable three-dimensional network structure. Materials with the perovskite structure have the following four characteristics. Firstly, such materials possess excellent photoelectric properties, lower exciton binding energy, and high optical absorption coefficients (up to 104 cm^{-1}) [21]. Secondly, perovskite material as a light-absorbing layer shows excellent absorption properties [22]. Thirdly, the materials possess a large dielectric constant, and electrons and holes can be effectively transmitted and collected. Lastly, electrons and holes can be transmitted simultaneously over distances of 100 nm or more [7], [23].

Perovskite materials have also been extensively studied for their applications in solution-processed light-emitting diodes [24], [25] due to their superior advantages of high photoluminescence quantum yield (PLQY), excellent color purity, low-temperature solution processing, and high

carried mobility necessary for light emitting devices. External quantum efficiencies (EQE) of perovskite light-emitting diodes (PeLEDs) have increased from 0.1% - 20% [26]–[30].

As earlier mentioned, despite the high efficiencies recorded in PSCs and PeLEDs they still face performance and stability issues. Another major concern is structural stability, PSCs undergo structural phase transitions [19], from orthorhombic (γ-phase) to tetragonal (β-phase) at 160°K (-113°C) and finally from tetragonal at <330°K to a stable cubic (α-phase) crystal structure at 330°K (57°C) which is a favorable temperature range for most electronic devices [31], [32].

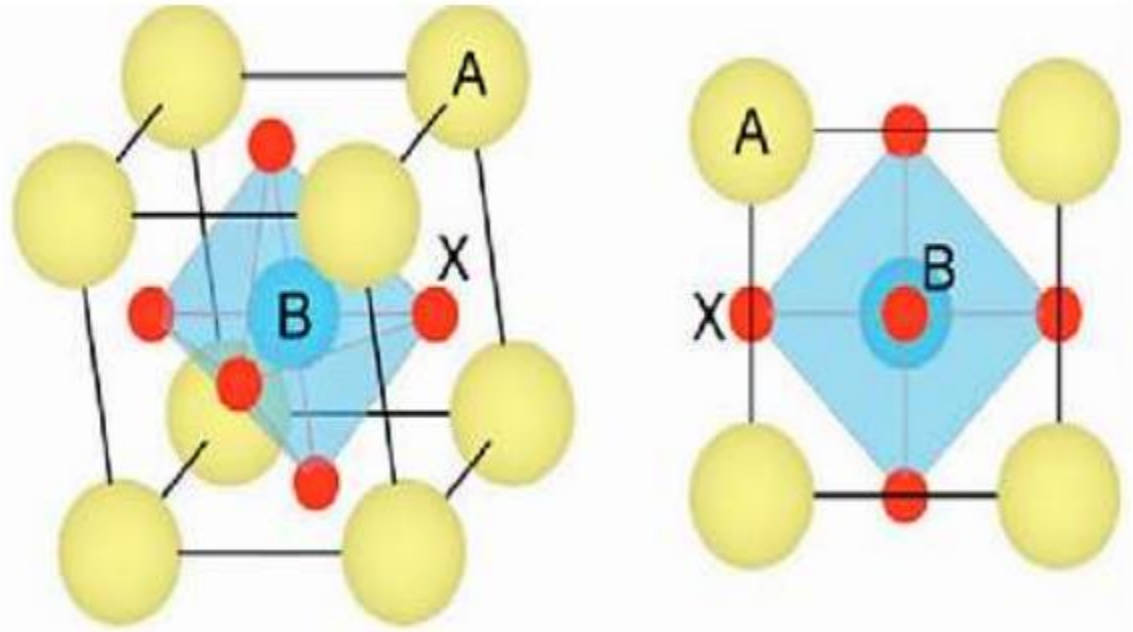

Figure 2.1: General Crystal structure of perovskite with ABX_3 formula [33]

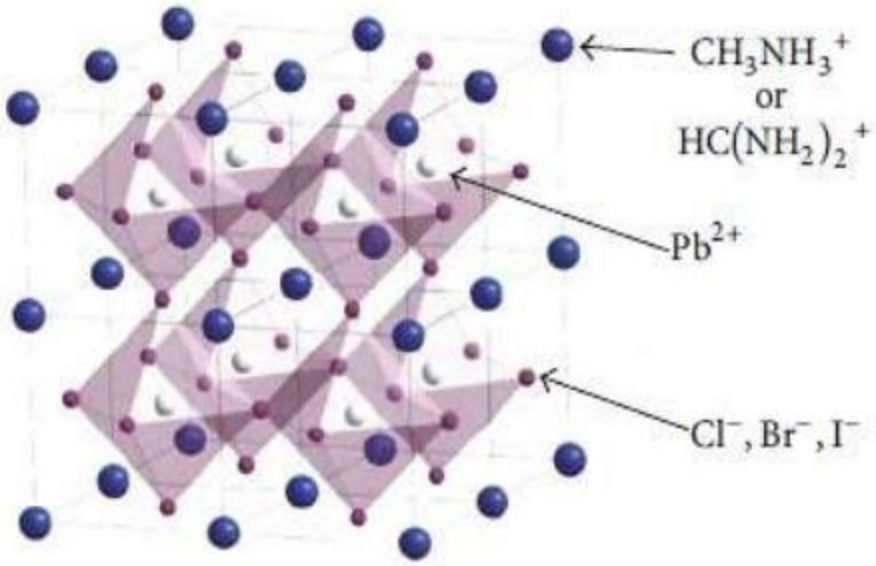

Figure 2.2: A Cubic lattice of perovskite structure Showing different materials on the A, B, and X site groups [23]

2.3.2 WORKING PRINCIPLE AND STRUCTURES OF PEROVSKITES AND OLEDs

A clear model of a PSC architecture is depicted by three main layers: a perovskite absorber layer, a hole transport layer (HTL), and an electron transport layer (ETL). The perovskite layer is sandwiched between the HTL and ETL [34]. These main layers are then sandwiched between the anode and cathode electrodes as shown in figure 2.3. The perovskite absorber layer is capable of absorbing solar radiation and generating excitons (electron-hole) pairs. The HTL and ETL provide a selective barrier on opposite sides of the perovskite layer permitting a selective flow of charge carriers to their respective electrodes [35].

Similarly, a clear and simplest OLED device is a dual injection light-emitting device composed of an emissive layer sandwiched between an anode and a cathode electrode [4]. For improved performance, additional layers are added to the single layer structure forming multilayer structures as in figures 2.5 b and c.

When an external voltage is applied to the OLED electrodes, the low work function cathode injects electrons while the high work function anode injects holes. The electron and holes recombine in the emissive layer forming electron-hole pairs (excitons) at bound energy levels. The excitons are deexcited and they release photons producing visible light. The reverse of this principle takes place in photovoltaic cells (PVC), absorption of photons by the absorber layer generates excitons, these excitons are dissociated at the active layer of the device and the electrons travel to reach the low work function cathode while holes flow to the high work function electrode. This flow of electrons to the cathode and holes to the anode leads to current flow. The principle of OPVs is the direct opposite of the principle of OLEDs figure 2.4 [36]

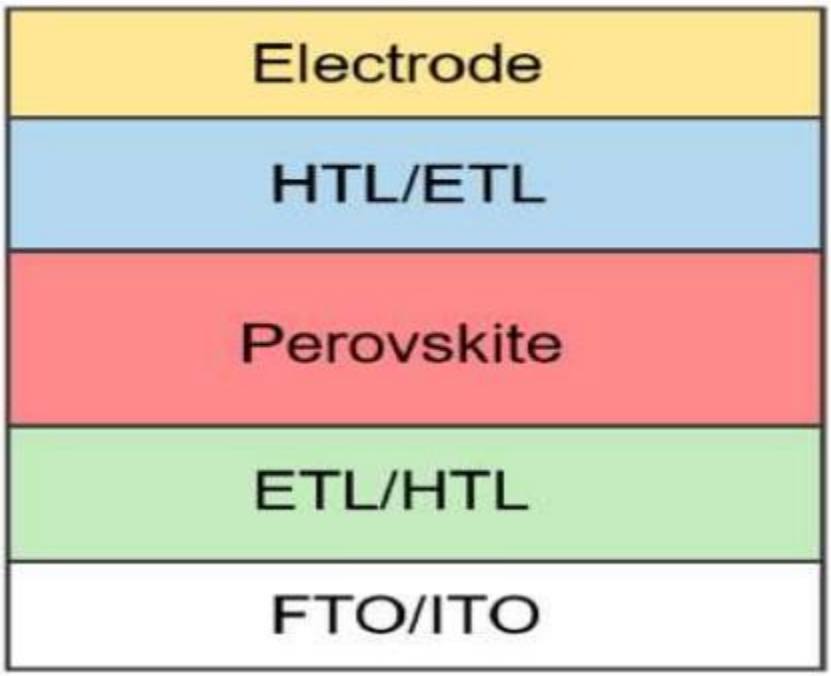

Figure 2.3: Typical structure of a perovskite solar cell (PSC) [37]

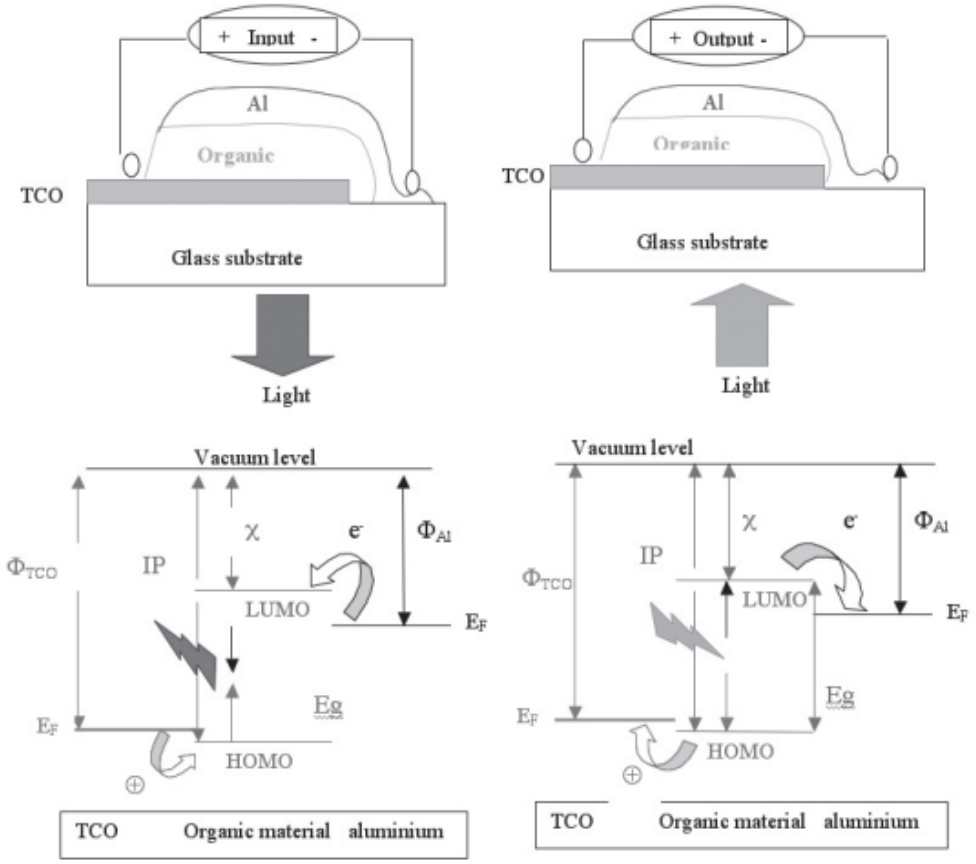

Figure 2.4 : Principle of an OLED (Left) and solar cell (right) (band scheme without contact) [36]

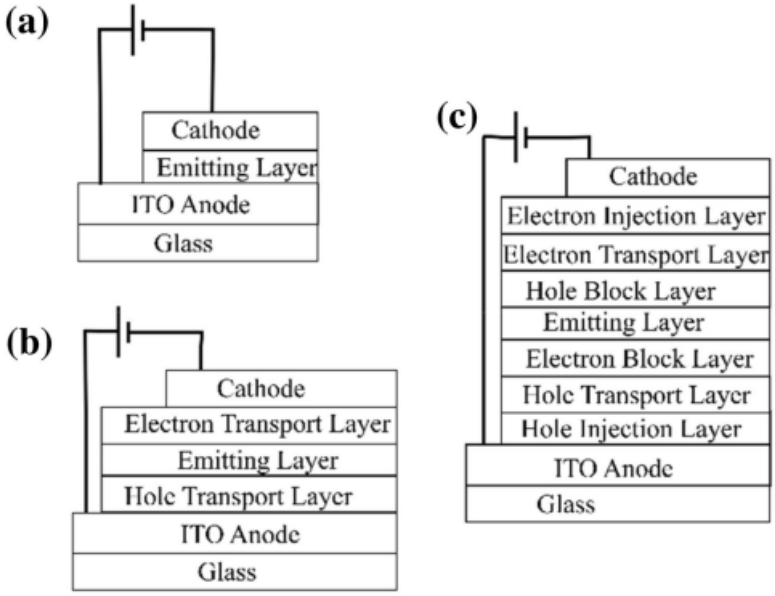

Figure 2.5: Schematic diagram of common OLED structure: a) OLED single-layer device structure, b) OLED three-layer device structure, c) OLED multilayer device structure [4]

In recent years, three main structures of PSCs have been extensively studied and developed: the mesoporous PSC (n-i-p), the planar PSCs (n-i-p), and the planar PSC (p-i-n) figure 2.7 a, b and c. The main difference between the n-i-p and p-i-n structures is that light penetrates the n-i-p structure via the ETL and the transparent conducting cathode lies in front of this ETL while in the p-i-n structure, light reaches the perovskite layer through the HTM with a transparent conducting anode in front of it.

2.3.2.1 Mesoporous Perovskite solar cell (n-i-p)

Mesoporous Perovskite Solar Cells (MPSCs) material has been extensively studied and widely applied because of its high porosity and large specific surface area (up to $1000m^2/g$). Other key attributes of MPSCs making them superior PSCs are low-cost materials, easy fabrication, and high PCE [34]. The application of mesoporous materials in perovskite solar cells allows the perovskite absorber to adhere to the mesoporous metal oxide framework to increase the light receiving area of the photosensitive material and improve the efficiency of the device [23]. From review work done by [34], a typical MPSCs has a compact layer or electron transport material (ETM) deposited on a fluorine-doped tin oxide layer (FTO), the ETM extracts only electrons while blocking holes. The perovskite layer is deposited on the nanopores containing ETL, this absorber covers it and penetrates it forming an intermediate mixed layer, the HTL and the top electrodes are sequentially deposited on the absorber layer forming a complete device.

In MPSCs, the most widely used ETM is TiO_2, other mesoscopic metal oxide materials used are: AL_2O_3, ZnO, SnO_2 [38], and ZrO_2 [33]. The TiO_2 as an ETM framework does not only form an interconnected stable absorber layer, it also transports electrons, blocks holes, and prevents

recombination of electron-hole pairs in the FTO substrate leading to improved performance of the device.

Hole transport material often used are Spiro-OMeTAD, poly(3-hexylthiophene-2,5-diyl) (P3HT) (2,2',7,7'-Tetrakis[N,N-di(4-methoxyphenyl)amino]-9,9'-spirobifluorene),Poly(3,4-ethylene dioxythiophene) polystyrene sulfonate (PEDOT:PSS). And materials often used as counter electrodes, are noble metals, such as Au, Ag, and Pt.

The main difference from the mesoscopic structure is that the planar structure removes the porous metal oxide framework. Two interfaces are formed between the perovskite materials and the two layers (the electron transport layer and the hole transport layer). Therefore, the electron-hole pairs are separated rapidly and effectively by the electron transport layer and hole transport layer, respectively.

2.3.2.2 Planar perovskite Solar cell (n-i-p)

Planar perovskites solar cells (PPSCs) have been investigated by many researchers due to some unique attributes such as low cost, easy processing, low-temperature process, and low cost [1]. The planar n-i-p PSC architecture has a compact ETM layer that is not intermixed with the perovskite layer as in the mesoporous architecture. Only two interfaces exist, the ETL/ perovskite and perovskite /HTL interface, this makes electron-hole(e-h) pairs to be separated more effectively and rapidly by the ETL and HTL [1].

2.3.2.3 Planar perovskite Solar cell (p-i-n)

The inverted PPSCs structure (p-i-n) shows great potential for better performance and flexible PV device applications due to their easy processing techniques, negligible hysteresis, and high stability [1]. The p-i-n PSC architecture is referred to as an inverted planar structure because the extraction

layer of a carrier is inverted in comparison to the n-i-p planar structure. The p-i-n planar architecture is built with a compact HTL.

Inverted PSC structures use semiconductor-organic material as both ETM and HTM layers. Many strategies such as crystalline regulation of perovskite, new perovskite composition, modification of charge carriers' transport layers, and geomorphology control have been used to optimize inverted PSCs performance.

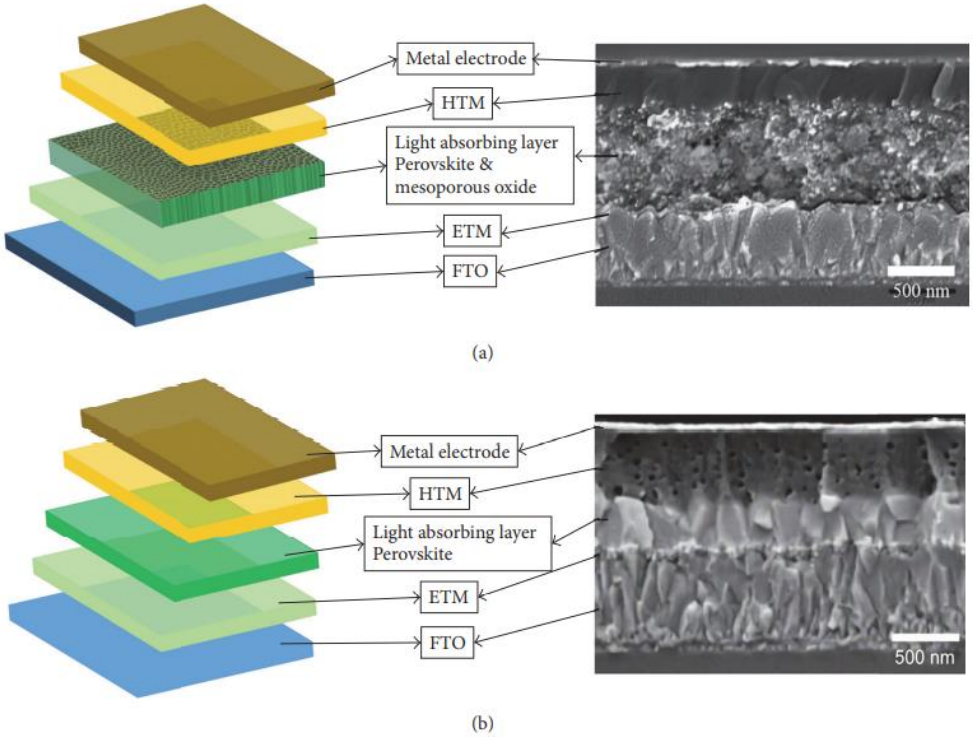

Figure 2.6: Schematic diagram and SEM section image of a) mesoscopic PSC architecture and b) planar heterojunction PSCS structure [23].

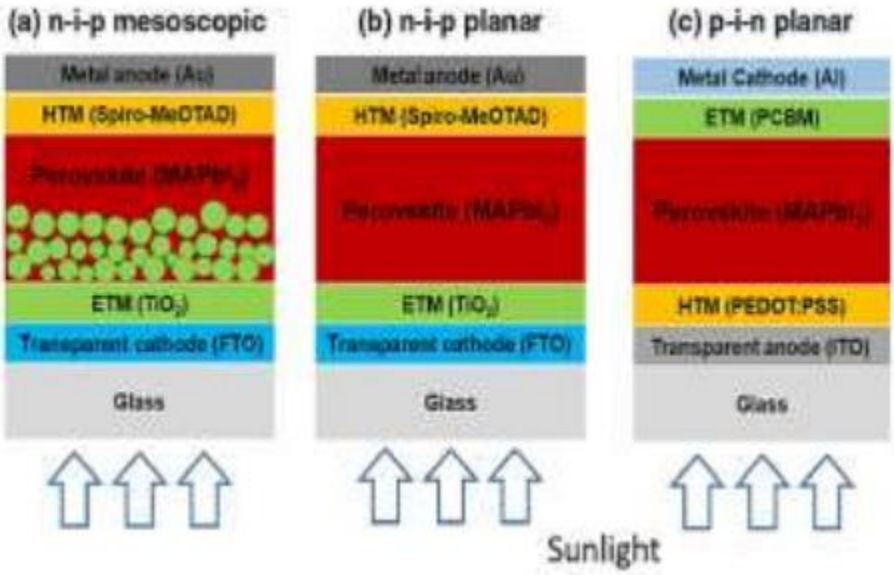

Figure 2.7: Schematic diagram of PSCs in the a) n-i-p mesoscopic, (b) n-i-p planar, c) p-i-n planar [39]

2.4 INSTABILITY OF PEROVSKITE LAYER OF PSCS.

Despite the high-power conversion efficiencies of PSCs compared to traditional solar cells, the long-term stability of the perovskite layer is still a major impediment to commercialization. The perovskite layer is unstable under severe environmental conditions such as; humidity, thermal treatment, light illumination, etc, leading to degradation [1]. Instability can also be due to adverse weather conditions, and exposure to oxygen. The overall effect of this degradation is the poor performance of the entire device. Crystal structure stability and environmental stability are the major stability challenges in perovskites.

2.4.1 Crystal structure stability:

Perovskites are known to exhibit different phase transitions; orthorhombic to tetragonal and tetragonal to cubic. Changes in the crystalline phase of organic-inorganic hybrid perovskites under

the influence of environmental conditions such as temperature, pressure, moisture, and its own properties affect the stability of PSCs. According to [40], during typical solution processes for perovskite fabrication, annealing is employed for the formation of the perovskite crystal structure, this thermal treatment has some effects on the crystal structure, decomposition of perovskite, and thermal stability of the HTM layers. The crystal structure coupled with the phase transitions determines the properties of the perovskite material. The tolerance factor (t) proposed by Goldschmidt (1927) is used to study the stability of ABX_3 perovskites. The tolerance factor is defined as:

$$t = \frac{r_A + r_x}{\sqrt{2}\,(r_B + r_x)} \qquad (2.1)$$

where r_A,r_B and r_x are the ionic radii for the ions in the A, B, and X sites, respectively [40]. The tolerance factor is a major determinant for the formation of stable perovskite structure, it restrains the ionic radius of the crystal structure. A well-packed cubic crystal organic-inorganic perovskite structures have a tolerance factor of t=1, they form hexagonal structure when t>1, orthorhombic for t<0.8, and cubic structure when 0.8<t<1 [41]. Non-perovskite structures have t>1 or t<0.71.

Variations in symmetry caused by octahedra tilting which corresponds to both temperature and pressure effects affect the electronic and optical properties of perovskite,[42] and thus influence photovoltaic devices' performance. Symmetry increases with temperature and t [40]. A lower tolerance factor than the recommended range leads to a reduction in symmetry, consequently, the perovskite structure will change to tetragonal or orthorhombic which has a negative effect on the optoelectronic properties.

2.5 Environmental stability (oxygen and moisture, UV light, solution process, temperature)

In PSCs, the perovskite films undergo a series of chemical reactions under the influence of different atmospheric conditions which are a major source of instability in PSCs. Moisture, oxygen, temperature, UV light, and solution process (solvents, solutes, additives), are key environmental factors under which perovskite films are susceptible to before or during use, and they lead to different problems of chemical stability of PSCs. For illustrative purposes, methylammonium lead iodide will be used as an example to discuss environmental stability issues. A major equation depicting the synthetic process (positive direction) of MAPbI and the decomposition (negative direction) of the perovskite is shown below in reaction (1).

$$PbI_2\ (s) + CH_3NH_3I\ (aq) \leftrightarrow CH_3NH_3PbI_3\ (s) \quad (1)$$

In a study by [43], it was verified that moisture and oxygen in the atmosphere can lead to irreversible degradation of MAPbI as in reactions (2 – 5) below. MAPbI is very sensitive to water, it hydrolyses in the presence of moisture leading degradation of the perovskite films. UV radiation is also a major cause of the degradation process. UV radiation leads to photochemical reaction (5) where HI decomposes to H_2 and I_2, and the consumption of HI in (4) and (5) moves the degradation process forward [40]. Some researchers showed that $CH_3NH_3PbI_3$ is more sensitive to moisture than $CH_3NH_3PbBr_3$. Hitoshi and co-workers proposed reactions (6-8) as a possible mechanism to explain the degradation of perovskite film under light exposure.

$$CH_3NH_3PbI_3\ (s) \leftrightarrow PbI_2\ (s) + CH_3NH_3I\ (aq) \quad (2)$$

$$CH_3NH_3I\ (aq) \leftrightarrow CH_3NH_2\ (aq) + HI\ (aq) \quad (3)$$

$$4HI\ (aq) + O_2\ (g) \leftrightarrow 2I_2\ (s) + 2H_2O\ (l) \quad (4)$$

$2HI\ (aq) \leftrightarrow H_2\ (g) + I_2\ (s)$ (5)

$2I^- \leftrightarrow I2 + 2e^-$ [at the interface between TiO2 and CH3NH3PbI3] (6)

$3CH_3NH_3^+ \leftrightarrow 3CH_3NH_2 \uparrow + 3H^+$ (7)

$I^- + I_2 + 3H^+ + 2e^- \leftrightarrow 3HI \uparrow$ (8)

Some common methods employed for improved stability in PSCs and OLEDs are encapsulation, controlled humidity fabrication [44], encapsulation in a nitrogen atmosphere [45], and the addition of a UV filter in front of TiO_2 to prevent UV degradation [46].

2.6 PEDOT:PSS AS A HOLE TRANSPORT MATERIAL FOR PSCs AND PeLEDs/ OLEDs

PEDOT:PSS [poly (3,4-ethylene dioxythiophene): polystyrene sulfonate] is an organic HTM that is commonly used in PSCs and OLEDs. PEDOT:PSS has advantages of high transparency, good conductivity, low hysteresis, tunable work function, good mechanical flexibility, and can be easily prepared in solution. It has been used as a dopant-free HTM in inverted (p-i-n) planar PSCs. However, due to a rather huge energy barrier between PEDOT:PSS and the active layer or emissive layers coupled with the high acidity of the PEDOT:PSS, the photovoltaic performance and stability are comparatively low. This also contributes to low open circuit voltage (V_{oc}), and short circuit current (J_{sc}). In addition, the PEDOT:PSS chain is hydrophilic, which makes it very difficult for the solution to be directly deposited on the photoactive layer which is hydrophobic. Although, PEDOT:PSS is capable of reducing the surface roughness of electrodes and the energy barrier between electrodes and perovskite material, the acidic nature of the solutions is still an issue to be addressed as it is capable of eroding the surface of the electrodes or layers it is deposited on[47]. Furthermore, despite the good work function of 5.2 eV, which is essential for proper hole injection

and transport, exciton quenching takes place at the PEDOT:PSS/perovskite interface [48]. Therefore, there is a need for doping or modification of PEDOT:PSS forming blends with improved properties which will yield optimum performance for applications in PSCs and OLEDs.

Transition metal oxides (TMOs) such as molybdenum trioxide (MoO_3), WO_3, and V_2O_5 have been extensively studied as substitute or modifier p-type semiconductors materials for PEDOT:PSS. Amongst these oxides, molybdenum trioxide having a high work function is the most studied HTM for applications in LEDs and OPVs [39, 40]. MoO_3, has been used to enhance the hole injection or transport in OLEDs [51], OPVs [42, 43], and PSCs [44, 45]. Several research groups have tried doping PEDOT:PSS HTL with MoO_3 to obtain better performances in their devices [46–48] and have reported promising results for improved performance on such devices.

2.7 NANOINDENTATION AND NANO SCRATCH TECHNIQUE

Nanoindentation is a non-destructive probing technique used for the investigation and characterization of the mechanical response of materials. Nano scratch on the other hand is a quantitative destructive technique in which critical loads at point(s) of failure are used to compare the cohesive or adhesive properties of thin films, coatings or bulk materials. This involves a material of know properties having contact with another material whose properties are under investigation. In this technique, an indenter tip with a penetration depth less than 500 nm ISO 14577-1 standards [9] is pressed onto the specimen and the penetration depth is continuously measured. This is a very common and robust technique based on the principles of contact mechanics which is often used to evaluate the mechanical properties of materials through surface measurements. This technique has evolved beyond measurements of just basic design parameters for materials such as hardness and Young's modulus to measurements of other parameters such as creep [10], yield strength [49, 51], and fracture toughness.

2.7.1 MEASUREMENT METHOD

Before any measurements, the sample must be prepared such that it is flat, smooth, and with parallel faces. A load is applied on the area of interest using an appropriate indenter to probe the material's surface to nm-scale depths. During the mechanical probing process, the load and penetration depth are simultaneously monitored and values are recorded with the help of high-resolution sensors and actuators. During the timed steady loading process, some materials exhibit timed-dependent behavior (creep), hence when the specified maximum force is reached, the process is halted for a dwell time to minimize material creep effects after which the indenter is released again in a controlled manner. The indentation depth is recorded continuously during the loading and unloading cycle. The results from an indentation test are transformed into a load displacement graph as in Figure 2.8. The absence of a dwell time leads to continuous deformation of the sample viscoplastically and this distorts the shape of the unloading curve thus leading to inaccuracies in modulus measurements. The unavoidable initial penetration is also a major issue to be taken note of to ensure accurate results.

For an indentation test, the indenter material must be 20% higher in hardness compared to the sample in order to generate plastic deformation [59]. Some indenter materials used are: Diamond, Tungsten Carbide, Cubic Boron Nitride, Boron Carbide, Sapphire, and Silicon Carbide. Common indenters Figure 2.8 used are: Vickers (pyramidal with square base), Berkovich (pyramidal with triangular base), cube corner (pyramidal with triangular base), spherical, and Knoop indenters, their properties and areas of applications are shown in Table 2.1. This technique provides data for optimizing the composition of materials structure and processing for thin films or bulk materials, it also aids in the comparative study of mechanical properties of thin films and bulk materials.

Table 2.1: Description of different indenter geometries and their applications in indentation.

Indenter Geometry	Details	Applications
Pyramidal	Triangular base Berkovich type indenter with an angle of 65.03^{o} between the axis of the pyramid (figure 2.9a) The square base Vickers indenter with an angle of 136^{o} between opposite faces of the pyramid	Measurements of mechanical properties like hardness, strain rate sensitivity for metals, ceramics and biological materials, internal friction [60]
Spherical	A variety of sizes exist ranging from 200µm to 1µm (figure 2.9b)	Suitable for plastics and polymers. This indenter geometry is good for investigating yielding phenomenon since the load changes slowly from elastic to elastic-plastic region.
Cyrlindrical	A flat tip indenter	Has a major advantage over other indenters of maintaining. constant contact area, however it is rarely used [61].

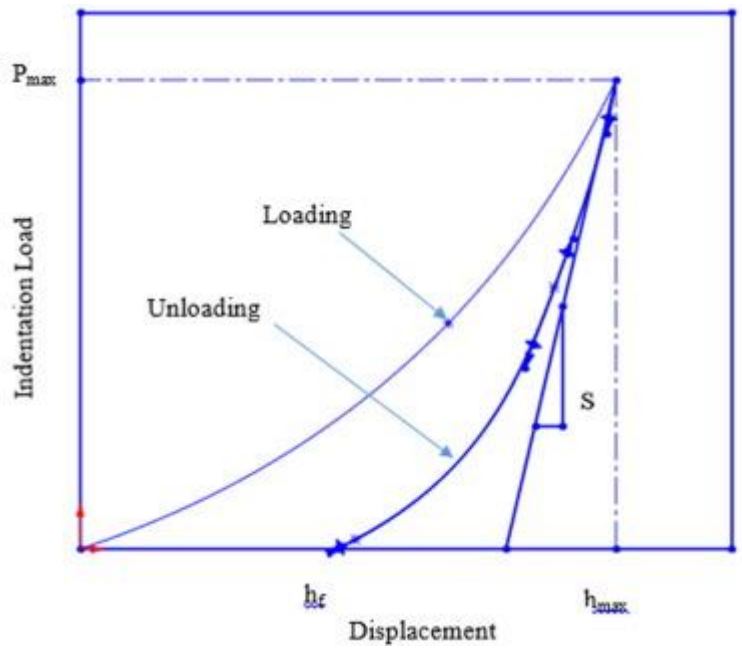

Figure 2.8: Load displacement curve for nanoindentation test [62]

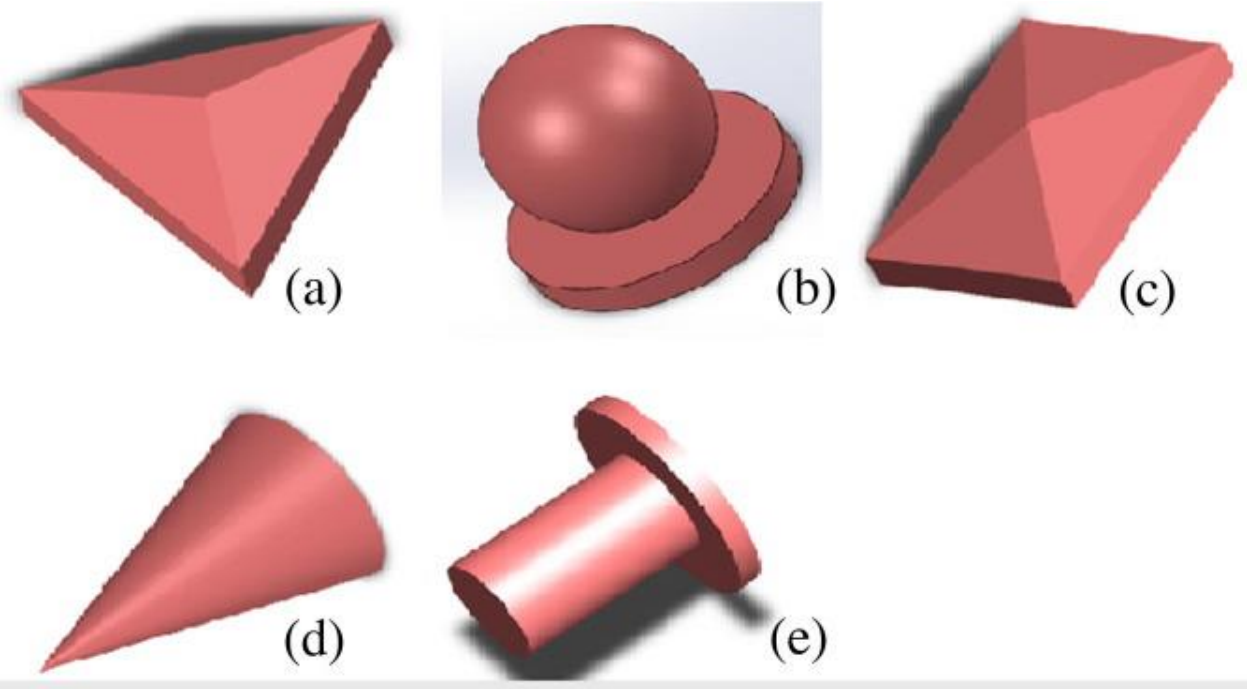

Figure 2.9: Indenter types: (a) Pyramidal Berkovich, (b): Spherical (c) Pyramidal Rockwell (d) Conical (e) Spherical [62]

2.8 ANALYSIS AND COMPUTATIONS FROM NANOINDENTATION DATA

The Oliver and Pharr (1992) method is the most widely used methodology for hardness and elastic modulus measurements. In this method, maximum load $P_{max,}$ maximum indentation depth $h_{max,}$ and the initial unloading contact stiffness 'S' (the slope of the upper portion of the unloading curve) are used as key parameters for contact depth (h_c) calculations. The shape and geometry of the indenter used play a major role in determining contact depth [63] . Mechanical properties are found by calculating the contact area (A_c) as a function of contact depth with the help of the load-displacement curve.

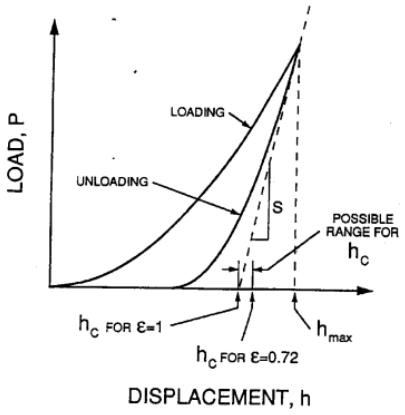

(a)

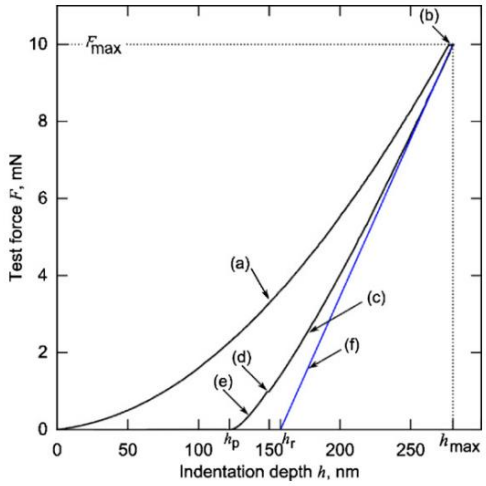

(b)

Figure 2.10: a) Load displacement curve and (b) Test force vs indentation depth plot [64].

For contact depth calculations, according to Oliver and Pharr (1992)

$$h_c = h_{max} - \varepsilon \frac{P_{max}}{S} \qquad (2.2)$$

Where $\varepsilon = 0.72$ *for cornical indenter and* $\varepsilon = 0.75$ *for paraboloid of revolution.*

A modified equation for contact depth by [64] is shown below.

$$h_c = h_{max} - \varepsilon(h_{max} - h_r) \quad (2.3)$$

where depth h_r is the intercept of the depth axis by the tangent line to the unloading curve (figure 2.10b) and $\varepsilon = 0.75$ for Berkovich or Vickers indenter [64].

For calculations of hardness H

$$H = \frac{P_{max}}{A_c(h_c)} \quad (2.4)$$

where the contact area $A_C = \sqrt[3]{3}h_p^2 tan^2 65.3 = 24.5h_p^2$ for Berkovich indenter.

hp is the permanent deformation depth of test sample.

To determine the Indentation modulus E, firstly the reduced Modulus E_r, is estimated as:

$$E_r = \frac{\sqrt{\pi S}}{2\sqrt{A_c}} \quad (2.5)$$

From $E_r = (\frac{(1-V_s^2)}{E_s} - \frac{(1-V_i^2)}{E_i})^{-1}$ (2.6)

Therefore, the indentation modulus can be gotten from.

$$E = \frac{(1-V_s^2)}{\frac{1}{E_r} - \frac{(1-V_i^2)}{E_i}} \quad (2.7)$$

where E_r is the reduced modulus of indenter contact, v_i and v_s are the Poisson ratios, of the indenters and test samples respectively. E_i and E_s are the elastic modulus of the indenter and test sample respectively.

2.9 Nano scratch resistance:

This is currently the most widely used method for the testing and evaluation of the cohesive-adhesive properties of thin film materials and coatings. Mechanical durability of thin film devices

is significantly influenced by the adhesion of the films to the substrate and each other, parameters such as hardness and elastic modulus of these films and the entire device can not suffice as a measure of mechanical durability. Thus, there is a need for more robust test methods that simulate real in-service conditions very closely such as the nano scratch test method.

The nano scratch test is a quantitative destructive technique in which critical loads at point(s) of failure are used to compare the cohesive or adhesive properties of thin films, coatings, or bulk materials. In this test, an indenter tip under a normal force is pulled over the surface of a specimen under investigation. The scratch test can be done by applying forces in steps or continuously with a linear increase. The forces used are usually from tens to hundreds of millinewtons with the corresponding displacements in several nanometers to hundreds of nanometers [65].

Stress fields initiated by the moving indenter leads to different failure modes: through-thickness cracking, coating detachment, plastic deformation, and substrate or film cracking. These failure modes are associated with cohesive failure of coating and substrate or adhesive failure of substrate and coating. This test is carried out to investigate critical loads (Lc) for which characteristics failure occurs and the results provide information on the adhesive and cohesive properties and tribological resistance [66] of the thin films or coatings.

During the nano scratch test, three detection techniques are used to detect critical load.

Detection of Sudden changes in penetration depth: The position of the stylus is usually recorded during the scratch test by a sensitive depth sensor, abrupt depth changes are correlated to coating chipping or delamination.

Friction probe: The ratio of friction to the normal force which is the coefficient of friction, can also be monitored during the test. A gradual increase in the coefficient of friction can be associated with ploughing while sharp variations are linked to fracturing or catastrophic failure [67].

Acoustic emission probe: An acoustic emission signal arises from the sudden release of elastic energy. Even slight cracking of the coating or thin film during the scratch process generates a shock wave. Such little cracks might not be detectable through microscopic methods.

2.10 REVIEW OF PREVIOUS WORK DONE ON THIN FILMS WITH NANOINDENTATION.

Dopant free PEDOT:PSS has been successfully used as HTM in PSCs [68], but underlying issues of acidity of the solution [47], exciton quenching at the HTL/perovskite interface [48] leading to low device performance are some measure challenges that have necessitated the use of dopant to enhance the properties and performance of these materials. Tsui and Pharr [69] used experimental methods to study the effects of substrate on the measurements of mechanical properties of thin films by nanoindentation using a model soft film on a hard substrate system: aluminum on glass. They used standard nanoindentation techniques to study the hardness and modulus as a function of indenter penetration depth of different aluminum film thicknesses (240, 650, and 1700 nm) deposited on glass. Hardness impressions from SEM and AFM images showed significant enhancement in indentation pileup in the aluminum film by the substrate. It was also reported that, the substrate affects the form of the unloading curve in a manner that has important implications for nanoindentation data analysis procedures. Due to these effects, nanoindentation measurements overestimates the film hardness and elastic modulus by as much as 100% and 50% respectively with dependence on the indentation depth. Findings also showed that greater errors occurred at depths approximately equal to the film thickness.

Ohmura and coworkers.,[70] used nanoindentation to study the load-displacement behavior of pure aluminum, gold and platinum thin films (0.1-3um) deposited on sapphire single crystals. The load penetration depth curves were analyzed using three different kinds of equipment's to investigate the deformation behavior of the thin films. Results showed that, with the use of Berkovich indenter, plastic deformation is constrained by hard substrate at penetration depths deeper than about one-fifth of the film thickness. The pop-in phenomenon common in aluminum films was considered to be caused by the natural oxide layer on the film surface, owing to the fact that decohesion of such thick films might not happen during the indentation process. The equipment dependence of the results obtained were found to be within allowed experimental error limits.

In an effort to understand the effect of pile-up on the mechanical properties of soft films on hard substrates, Saha and Nix [71], studied the indentation properties of sputter deposited W thin films on single crystal sapphire substrates. A Nano XP^{TM} was used to determine the hardness and elastic modulus of the films via nanoindentation. To determine the hardness and modulus, the Oliver and Pharr method was first used and this method does not account for pile-ups that occur along the flat faces of the indenter. In a second method was based on the fact that W and sapphire have very similar elastic moduli allowing the film/substrate composite to be treated as an elastically homogeneous. It was then possible to determine the true contact areas directly from the measured contact stiffness and from that determine the true film properties. This method also provided a quantitative estimate of the pile-up height which compared well with direct AFM measurements of the pile-up height. Using nanoindentation, Alcala et al,.[72] determined the hardness and Young's modulus of barrier-type amorphous anodic oxides. They carried out shallow indents of 55 nm depth on, alumina, tantala and alumina/tantala mixed oxide films of about 500 nm thick. The alumina, tantala and alumina/tantala hardness measurements were approximately 7.0, 5.3, and

6.5 GPa respectively and with respective elastic modulus of approximately 122, 140 and 130 GPa. These results revealed opposite trends, with alumina having highest hardness but lowest elastic modulus and the mixed oxide having intermediate properties. Comparing these hardness and elastic modulus of anodic alumina to crystalline forms of alumina, it was found that the values are low, with reduction by factors approximately in the range of 3.1- 3.7. A review by Bull [73], he briefly reviewed developments in numerical simulations and extended recent modeling developments in energy based predictive model for the hardness and Young's modulus of a coated system. Predictions of the model could be greatly improved by taking into consideration the fracture behavior of the coating during the indentation process. To fully understand the deformation mechanisms and the system properties, evidence for fracture can be obtained from load displacement curves gotten through nanoindentation, and high-resolution microscopy imaging. A combination of FEM and other predictive models are essential to fully understand mechanical properties of a coating/substrate system for better selection and optimization. [74] reviewed and discussed mechanical property measurements using nanoindentation techniques with emphasis on the use of sharp indenter tips and how they can be used to measure hardness, elastic modulus, continuous stiffness, scratch resistance, film-substate adhesion, residual stresses, time dependent creep and relaxation properties, fracture toughness, and fatigue. The applications of continuous stiffness measurement (CSM) technique for nanoindentation for layered materials and non-homogeneous composites. Also, they reviewed recent progress in development of the nano-fatigue measurement technique and the future prospects for research in nanoindentation are also discussed. Shan and Sitaraman [75] in a study of elastic-plastic characterization of thin films by nanoindentation technique presented a methodology that combines both nanoindentation and finite element modelling to characterize the elastic and plastic properties of a titanium thin film on a

silicon substrate. In this study, both experimental and FEM results revealed that, the Young's modulus of the titanium thin film did not change much compared to the bulk titanium film. Results also indicated that, plastic properties (yield stress and strain hardening exponent) of the thin film were higher compared to those of the bulk titanium. Fang et al., [76], used scanning probe microscopy (SPM) and nanoindentation techniques to investigate TiC, TiN and TiCN thin films deposited on silicon by plasma enhanced chemical vapor deposition (PECVD). Results indicated that the TiC films exhibits lower surface roughness and friction coefficient compare to the TiN and TiCN films. Results also showed that, for all the thin films, the Youngs's modulus and hardness both decreased with increasing indentation depth with the TiC film showing higher hardness and Young's modulus. A contact stress-strain relationship via nanoindentation depicted that the TiC film can bear larger indentation loads and possess a lower surface strain within a nanometer-scale. Xia et al. [77], used nanoindentation and Vickers microindentation to measure the young's modulus, hardness and fracture toughness of highly ordered nanoporous alumina (PAA). In this study, a FE model which takes into account the anisotropy of pores was developed and used to extract values of the Young's modulus and hardness from experiments. Their measurements showed that, heat treatment of 650^{o}C caused an increase in the hardness from 502 to 6.3 GPa, while the fracture toughness decreased sharply from 3.4 to 0.4 MPa-m$^{(1/2).}$ However, this same heat treatment did not affect the Young's modulus of 140 GPa. They also observed that, when indentation are made on the top surface of the membrane, nanopore collapse in shear bands instead of through crack formation around the indent. This results suggested that, the nanopores greatly improved the toughness of the porous alumina in the transverse direction. XRD curves showed no signs of phase change in the amorphous alumina to crystalline phase after annealing at 650^{o}C. From the FTIR spectra, it was observed that the heat treatment greatly reduced the OH

content of the alumina. This significant loss in OH during annealing caused a change in the amorphous structure which was attributed to the sharp decrease in fracture toughness observed. Bressan et al., [78], investigated the nanoindentation process on thin films and bulk materials by numerical simulation of using ABAQUS. Thin films and bulk materials of pure copper, titanium and iron were simulated considering hardening law. The numerical results obtained from simulations of these materials were in good agreement with experimental results. However, simulation results depended very little on frictional coefficient but were significantly dependent on the mesh size, indenter tip radius and the hardening law imposed on the model. In a dimensional analysis and FE modeling conducted by Ni and Cheng [79], to examine conical indentation in homogeneous materials and hard films on soft substrates, the solid material model followed the incremental theory of plasticity with Von-Mises yield surface. On examining the validity of the Oliver and Pharr method for hard films on soft substrates, they reported that, this method was valid only when the indentation depth is less than 10% of the film thickness. They also observed in their study that for conical indentation in homogeneous materials and hard films on soft substrates, a linear relationship existed between the ratio of hardness to reduced modulus and that of reversible work to total work. This relationship can be used to deduce hardness, reduced modulus, and contact area for instrumented conical indentation in homogeneous and coated materials. Huang and Pelegri [72,73], employed nanoindentation and FE to characterized and calculate the mechanical properties of a thin film material system of oxidized silicon grown on silicon substrate. Infinite elements in finite element nanoindentation analysis are used to allow for actual specimen size simulation and produce accurate results. The hardness and reduced Young's modulus of the featured thermally oxidized silicon on silicon substrate were directly determined from Berkovich nanoindentation measurements as 9.23+- 0.30 GPa and 63.11 +- 0.26 GPa, respectively. The

hardness and Young's modulus obtained from the FE analysis were 10.63 GPa and 65.20 GPa respectively, with an initial yield stress of 6.50 GPa and poison's ratio of 0.35. It was also proven that the substrate, the friction coefficient between indenter tip and thin film surface, and the bottom boundary conditions have no influence on the FE analysis on the thin film for maximum displacements of indenter tip less than 10% of its thickness. Zhao et al.[82] in a study proposed a method that utilizes only the loading curves of an indentation test to extract the elastoplastic properties of an elastic-perfectly plastic thin film and even the plastic properties of of a work hardening thin film. Measurements were taken at two different indentation depths having different levels of substrate effects leading to the establishment of independent equations that correlate the materials properties with the indentation responses. This study also proposed an effective reverse analysis algorithm by which the desired film properties can be determined from sharp indentation test. Extracted materials properties agreed well with those measured from bulk materials. Li and Vlassak [83], developed a data analysis procedure to estimate the contact area in an elasto-plastic indentation of thin films bonded to substrate. The developed procedure can be used to derive the Young's modulus and hardness of the thin film using the load displacement, and contact stiffness data at indentation depths which are a significant fraction of the film thickness. Their analysis was based on Yu's elastic solution for the contact of a rigid conical punch on a layered half-space which uses an approach similar to the Oliver and Pharr method for bulk materials. Their demonstrated methodology for both compliant films on stiff substrates and the reverse combination showed improved accuracy over previous methods. Cabibbo et al. [84], measured and analyzed the indentation hardness of SiO_2 coating by both visual and analytical methods. The scanning probe microscopy-based direct measurement method revealed quite good qualitative and quantitative literature data correspondence. The method was therefore developed and improved to

make it dependent on curve parameters, such as applied load and penetration depth, rather than on direct SPM measurements of the contact area. Their study also discussed a correlation of the pile up phenomenon to the m exponent of the load relationship.

Zhang [85], used nanoindentation and FE method to determine the mechanical properties of YBCO thin films deposited on SrTiO3 (100) substrates by magnetron sputtering. A Berkovich indenter and scanning electron microscopy was used. The hardness and Young's modulus of the thin films were determined from indentation load-depth curves through the Oliver and Pharr method. Indenter size effects due to surface roughness were observed in SEM images, consequently, the hardness values of the YBCO thin films also showed depth dependence. An effective analytical method that accounts for indenter imperfections was proposed and results for the elastic modulus, yield stress, and friction angle were validated by experimental data.

ElMahmoudy et al.,[86] investigated the effect of 3-glycidoxypropyltrimethoxysilane (GOPS) content in PEDOT:PSS dispersions films spun cast from these formulations. It was found that the concentrations of GOPS had tremendous, yet gradual impact on the electrical, electrochemical and mechanical properties of the PEDOT:PSS /GOPS films with an optimum concentration which maximizes a specific feature of the film such as its water uptake or elasticity. The GOPS aided in obtaining better mechanical integrity in the aqueous media with high conductivity. Their results showed that, additives life GOPS can enable superficial co-optimization of electrical and mechanical properties for bioelectronics applications. Alaboodi and Hussain [62], in a review article presented a detailed procedure of nanoindentation experiment and its finite element analysis, latest developments in this areas are also provided with a focus on thin films.

Zhang et al.,[87], in an experimental study to investigate the thickness-dependent hardness of three SiO_2 thin films (500 nm, 1000 nm, and 2000 nm) thicknesses on Si substrates using

nanoindentation, found that the average grain size of SiO_2 thin films observed by atomic force microscopy increased with increasing film thickness. Nanoindentation results for hardness also showed that the average intrinsic hardness decreased with increasing film thickness and grain size, a similar trend with the Hall-Petch relationship. For all three SiO_2 thin films thicknesses: 500 nm, 1000 nm, and 2000 nm, the same comparative depth range of ~0.4 – 0.5 existed, above which the intrinsic hardness without substrate influence can be determined. Jebur et al.[88] investigated the effects of graphene on the structural, morphology and optical properties of PEDOT:PSS thin films and found that: The spin coated nanocomposite films on pre-treated glass consisted of PEDOT:PSS and graphene of different weight percentages (0.5, 1, 1.5, 2) wt% as a dispersion phase. AFM results showed increased roughness by about 92% through the roughness average (Sa) and 45% through the density of summits(sds) parameter. This was proven in the SEM images which showed that PEDOT: PSS films without graphene had a smoother surface compared to those with graphene confirming clear and significant improvement mechanical strength of the prepared films.

CHAPTER THREE

3.1 MATERIALS AND METHODOLOGY

The methodology described for this project work was mainly experimental coupled with some analytical computations and modelling of data to obtain mechanical and electrical properties. The materials, equipment's, experimental and computational analysis employed are described below.

3.1.1 Materials Description

1.3 wt% aqueous, conductive grade PEDOT:PSS [poly(3,4-ethylenedioxythiophene)-poly(styrene sulfonate)] and Molybdenum (VI) oxide (MoO_3) nanoparticles were purchased from SIGMA-ALDRICH Co,3050 Spruce Street, ST Louis USA. Acetone; Isopropyl Alcohol (IPA), Aqueous ammonia solution was purchased from Trust chemical laboratories (TCL), distilled water. Fluorine-doped tin oxide (FTO)-coated glass.

3.1.2 Equipments Used

Brewer Science Cee 200X Precision Spin coater; Hysitron TI 950 Triboindenter Nanoindenter from Bruker; (Hysitron, Inc USA), Lucas/Signatone SP4, S302 Four-point Probe and KEITHLEY Source meter. Magnetic stirrer, hot plate, glass cutter, nitrogen gun, glass cleaning jar, precision weighing balance.

3.2 EXPERIMENTAL PROCEDURE

The aqueous PEDOT:PSS and MoO_3/PEDOT:PSS hole transport layer materials were spin coated on normal glass and on FTO-coated glass substrates. Firstly, the glass cutter was used to cut 15mm x 15 mm of normal glass and FTO-coated glass substrates. The normal glass and FTO-coated glass substrates were cleaned sequentially in detergent, distilled water, acetone and IPA with sonication for 5minutes in each liquid medium and annealing at 110 ^oC for 10minutes to remove any moisture.

With reference to literature reported by [58], the MoO_3/PEDOT:PSS composite blends of different MoO_3-ammonia ratios were prepared. Molybdenum trioxide nanoparticles were dissolved in aqueous ammonia to produce a 5mg/ml MoO_3-Ammonia solution. Pure PEDOT: PSS and the MoO_3-ammonia solution were mixed together at different volume ratios (1:0.1, 1:0.3, 1:0.5) forming PEDOT:PSS/MoO_3 blends. The prepared PEDOT:PSS/MoO3 blends were stirred for 1h before spin coating onto the substrates.

Spin coating process: The Brewer Science Cee 200x precision spin coater was used to spin-coat aqueous PEDOT:PSS and MoO3/PEDOT:PSS blends onto the glass substrate and on the FTO-coated glass. The PEDOT:PSS and MoO3/PEDOT:PSS blends of different compositions were spin coated on the substrates at 1000 rpm for 45 s, and thermally treated for 10mins at different temperatures: 60 ^oC, 80 ^oC, 100 ^oC and 120 ^oC.

3.3 SAMPLES CHARACTERIZATION

The mechanical characterization of the PEDOT: PSS, PEDOT: PSS/MoO_3-ammonia composite HTL for hardness and elastic modulus measurements was done using a Hysitron TI 950 Triboindenter Nanoindenter from Bruker. The sheet resistance measurements were taken with the help of a Lucas/Signatone SP4, S302 Four-point Probe and KEITHLEY Source meter. The surface morphology of the HTL films were observed with the help of SPM images from the Hysitron TI 950 Triboindenter which has an inbuilt SPM/AFM imaging capability.

A flowchart for the entire experimental process is as shown in figure 3.1 below.

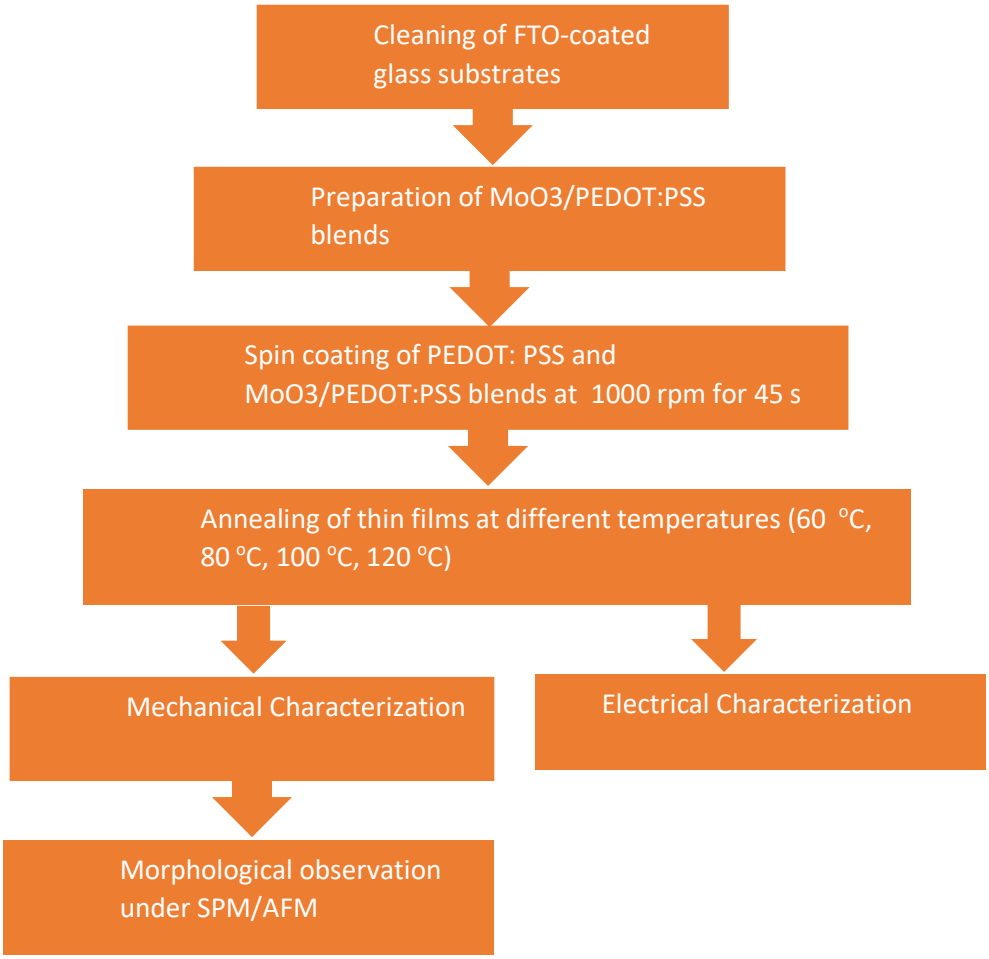

Figure 3.1: Flow chart of PEDOT: PSS, PEDOT: PSS/MoO_3-ammonia composite HTL preparation and characterization.

3.3.1 Mechanical Characterization

The mechanical characterization was carried out using a Hysitron TI 950 Triboindenter to measure the hardness and elastic modulus of both the PEDOT:PSS thin films and MoO_3/PEDOT:PSS blend thin films. The TI 950 Triboindenter is equipped with an optical camera system for imaging, TriboScanner for provision of fine scale positioning of the nanoindentation probe and also for performing in-situ SPM imaging of a sample surface before and after indentation test, and a probe for indentation of the sample figure 3.2. For this study, a Berkovich indenter tip, a three-sided pyramidal tip, was used for the indentation at a loading rate of 10 µN/s. The loading profile

consisted of three steps: firstly, loading to a peak load of 200 μN for 20 s, holding for 5 s and finally returning to zero load in 20 s. A dwell time of 5 secs was employed to minimize materials creep effects on measurements, before the unloading of the indenter from the sample. Multiple evenly spaced grid indentations were done on a selected area of the sample to test for the hardness and Young's modulus of the different thin film blends. The Oliver and Pharr method [63] discussed in chapter two can be employed for the estimation of the Young's modulus (E) and Hardness (H) of the samples. Further analysis of data for hardness and elastic modulus measurements were done and the results are discussed in chapter four.

3.3.2 Surface Morphology study

Imaging of the thin films was done with the help of the onboard optical camera as well as the TriboScanner which performed in-situ SPM/AM imaging of the thin film surfaces before and after the indentation during contact mode.

The images were analyzed with the help of Gwyddion software for a better view of the surface morphology of the different thin films from the images and also get their corresponding surface roughness data.

3.3.3 Study of the Distribution of Mechanical Properties

TriDiMap tool box in MATLAB was used to further investigate the phases present in the prepared thin films and to study the distribution of hardness and elastic modulus within these phases.

For the determination of the mechanical properties of each individual phase present for our composite material after the grid nanoindentation, the TriDiMap toolbox was used in MATLAB, to plot, map and analyze the nanoindentation dataset for the different samples. Results of the

TriDiMap analysis for the different samples using the nanoindentation dataset are presented in chapter four.

CHAPTER FOUR

4.1 RESULTS AND DISCUSSIONS

4.2 SURFACE MORPHOLOGY OF PEDOT:PSS AND MoO_3/PEDOT:PSS BLENDS

AFM images of thin film blends were taken before and after the indentation with the help of a contact-based scanning probe technique. The optical microscopy images for the as-prepared PEDOT:PSS and MoO_3/PEDOT:PSS blend HTL of different compositions thermally treated under four temperature regimes are presented in figure 4.1. The as-prepared PEDOT:PSS samples fig 4.1a-d do not show any clear visible features for the different heat treatments except for a change in the colour of the films which signifies some changes within the thin films at atomic levels. Heat treatment of the MoO_3/PEDOT:PSS samples within the 60 ^oC and 80 ^oC temperature regimes, reveals high levels of crystal-like structures present in the MoO_3/PEDOT:PSS blends. However, further annealing to a much higher temperature regime 100^0C-120^0C, the high levels of crystallization observed in fig 4.1a and b is greatly reduced with little or no visible crystals **figure 4.1 g** and **h**. Thus, there is a clear significant modification of the thin film blend surfaces and microstructure under different annealing conditions with crystal growth more predominant in the lower temperature regimes. Samples with high doping levels such as in the 1:0.5 PEDOT:PSS/MoO_3 thin film blends, the changes in microstructure are clearly visible from the optical microscopy scans (4.1e- h), while in thin film blends with little MoO_3 doping (1:0.1 and 1:0.3), these microstructural changes are not very visible in figure 4.1a-d.

These observed changes in microstructures of the thin film blends can be attributed to the rapid bond formation taking place due to small atomic distances at lower temperature, nucleation and growth of small crystals. Increasing annealing temperatures generally increases crystal growth,

small crystals grow larger and coalesce forming a more densified system at higher temperatures. Also, the blended ratio of MoO_3 also affects bond formation, nucleation and growth of crystals at different temperatures.

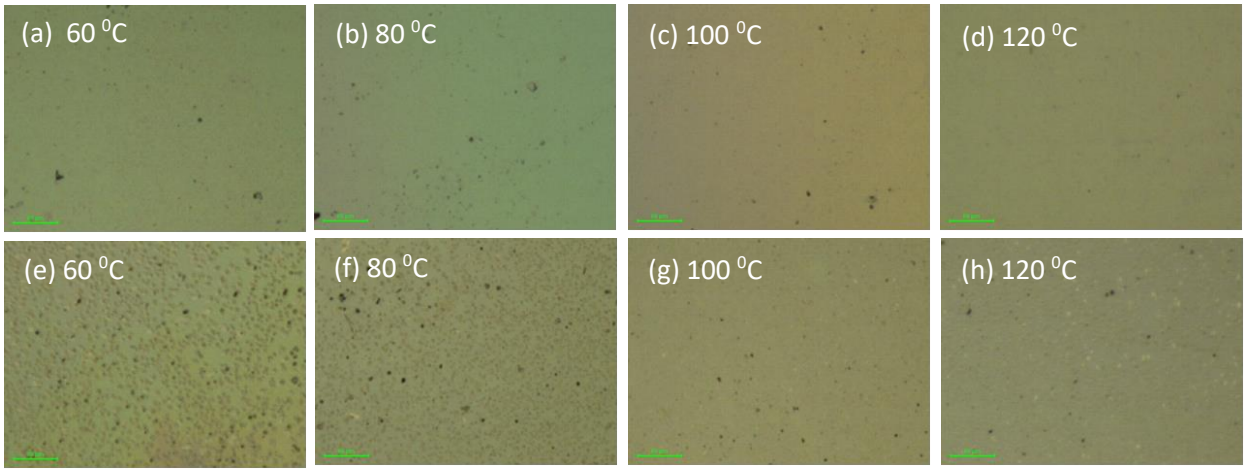

Figure 4.1: Optical microscopy images of different annealed PEDOT:PSS **(a) - (d),** and **1:0.5** PEDOT:PSS/MoO_3 blends (**e) – (h)**.

Typical two dimension (2-D) and 3-D surface profiles of atomic force microscopy (AFM) surface scans of the as-prepared PEDOT:PSS and PEDOT:PSS/MoO_3 blends are presented in figure 4.2. A major inconvenience to measuring of mechanical properties during nanoindentation especially at shallow depths is the surface roughness. Therefore, measurements of properties were done at indentation depths between 10 nm to 500 nm to minimize surface roughness effects. The values of the root mean square (RMS) surface roughness and mean roughness are summarized in table 4.1. The values of the surface roughness for the different thin film compositions are in order of nanometer, this indicate that all the PEDOT:PSS thin films and PEDOT:PSS/MoO3 blend thin films have a good smoothness, which ensures consistency and accuracy of the nanoindentation experimental results. Also, the root mean square surface roughness measurements show that samples with a very small percentage of dopants have better surface roughness compared to the

as-prepared samples and those with high dopants (50%). Low mean roughness is very important for multilayer devices which are of interest here, as high surface roughness can impede proper adhesion of layers and general performance of devices. High surface roughness also has a major consequence on injection and transportation of charges across different layers which reduces device performance as charges will have to travel longer distances.

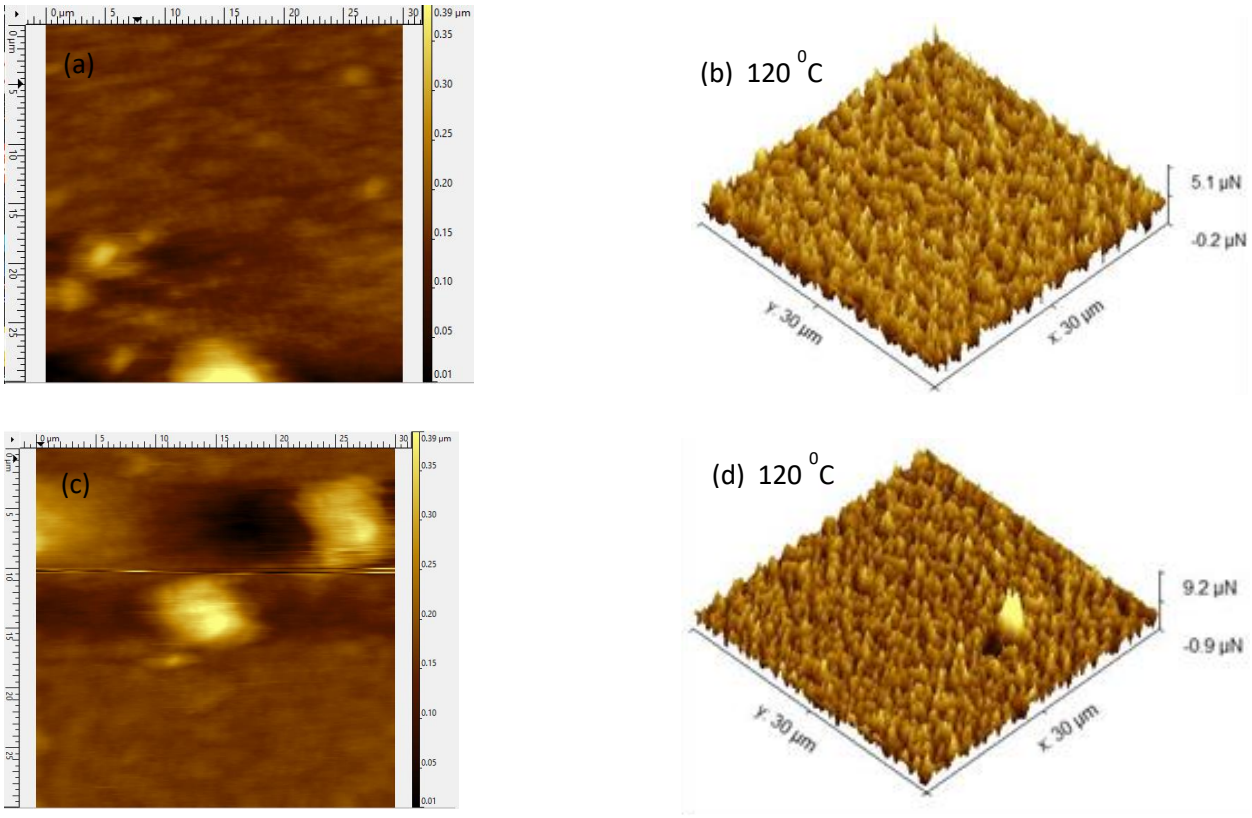

Figure 4.2: AFM images of different annealed thin films **(a)** 2-D AFM scan of PEDOT:PSS thin film (b) 3-D AFM image of PEDOT:PSS thin film **(c)** 2-D AFM image of **1:0.1** PEDOT:PSS/MoO_3 blend thin film (**d)** 3-D AFM image of **1:0.1** PEDOT:PSS/MoO_3 blend thin film

Table 4.1: Surface roughness measurements for Pure PEDOT:PSS(CT) and PEDOT:PSS/MoO3 blend (1:0.1, 1:0.3, 1:0.5) thin films on FTO-glass at different annealing temperatures.

Sample	Composition PEDOT:PSS/MoO_3-ammonia	Annealing Temperature (^oC)	RMS Roughness (nm)	Mean Roughness(nm)
CT	1:0		8.450	6.566
	1:0.1		12.0492	7.6514
	1:0.3	60	13.2119	8.9294
	1:0.5		51.2672	40.2754
CT	1:0		7.3400	5.57547
	1:0.1		11.1223	8.7435
	1:0.3	80	11.4702	8.2883
	1:0.5		60.3395	48.8060
CT	1:0		10.8563	8.0654
	1:0.1		9.02296	7.04769
	1:0.3	100	34.2699	18.6993
	1:0.5		32.6017	23.2349
CT	1:0		7.21787	5.60687
	1:0.1		12.9346	8.9912
	1:0.3	120	16.1522	11.1402
	1:0.5		38.7156	31.0287

There is a general reduction in surface roughness of the thin film blends as temperatures are increased from the lower temperature regime (60 – 80 ^{0}C) to much higher temperatures (120 ^{0}C). These reduction in mean roughness can be associated with the fact that, at higher temperatures; there is burn out of some materials leading to collapse and densification, diffusion rates also increase, there is more nucleation and growth with phase transformations taking place. These various phase transformations initiated by temperature increase give rise to the microstructural and morphological changes observed in the thin film blends within the different temperature regimes.

4.3 NANOINDENTATION RESULTS FOR HARDNESS AND YOUNG'S MODULUS MEASUREMENTS

Multiple load displacement curves as presented in figure 3.3 were obtained from the indentation data and a best fit was used for calculation of the Young's modulus and hardness. Indentation results for hardness and reduced Young's moduli obtained over a range of contact depths are presented in figures 4.3. The nanoindentation results discussed here is for indentation depths below 500 nm. These results suggest that there is no particular strong interdependence between the contact depth and the hardness or the reduced Young's modulus for the different volume ratios as presented in fig 4.3. However, from the measurements, optimum hardness and reduced Young's modulus for all samples were achieved at indentation depths below 500 nm. Hardness measurements at contact depths below 500 nm, show that, as-prepared PEDOT:PSS thin films has lower hardness compared to the MoO_3 doped thin films as expected. Maximum hardness value of about 5.3 GPa (for hc=39.1 nm) is measured for the 1:0.5 blended ratio within the 60 ^{0}C temperature regime, further annealing to 120 ^{0}C continuously reduces the hardness to about 2.3 GPa at ~61 nm. Also, PEDOT:PSS/MoO_3 blends with a composition of 1:0.3 shows improved hardness as annealing temperatures are increased from 60 ^{0}C to 120 ^{0}C. This improved hardness

in the hybrid thin films can be associated with the introduction of MoO_3 into the PEDOT:PSS leading to phase changes from crystalline at lower temperatures to amorphous at higher temperatures.

At indentation depths above 500 nm, the samples all show similar hardness values in all the annealing temperature regimes.

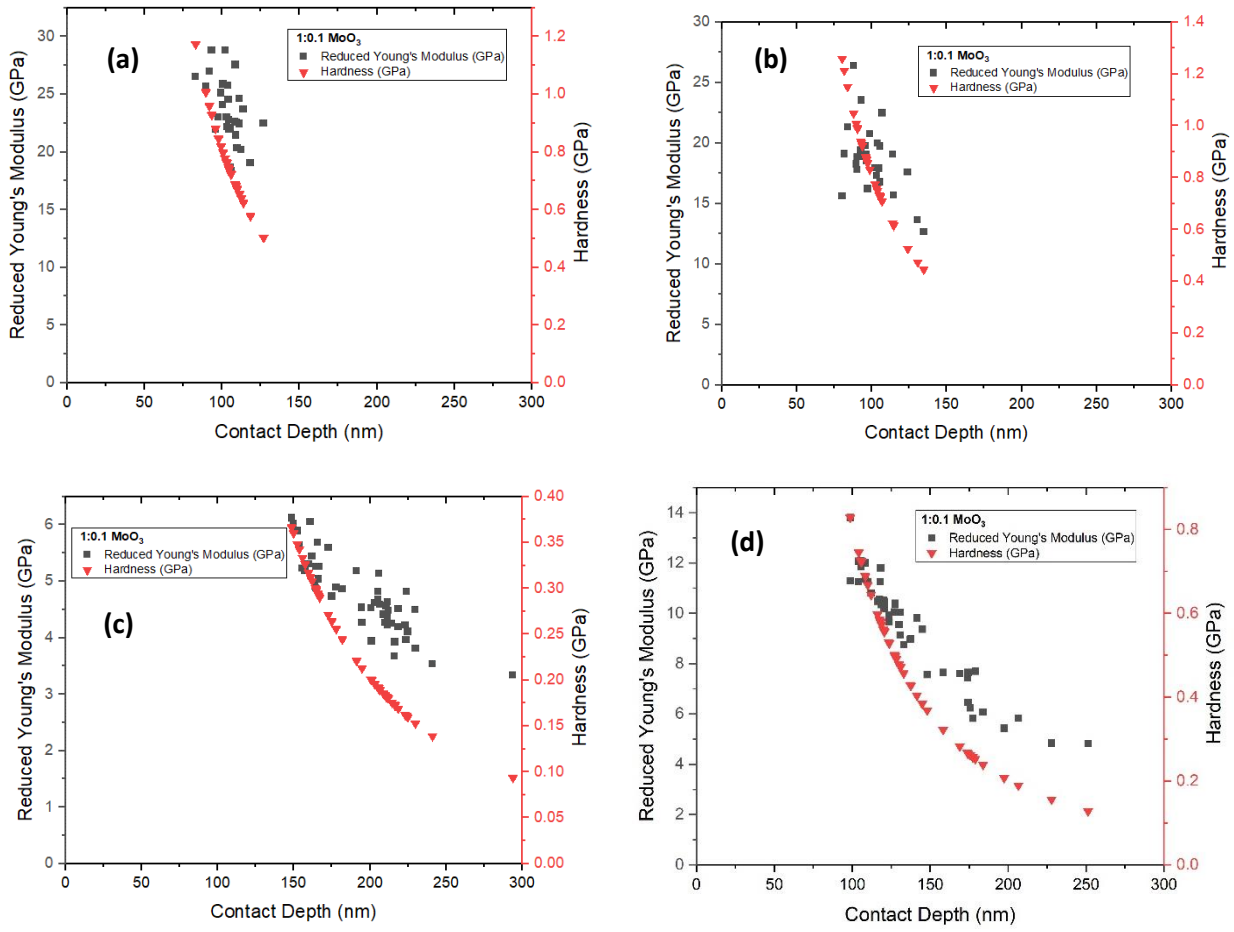

Figure 4.3: Reduced young's modulus and hardness of PEDOT:PSS/MoO_3 thin film blends [1:0.1] annealed at a) 60 ^{0}C, b) 80 ^{0}C, c) 100 ^{0}C and d) 120 ^{0}C, measured by nanoindentation.

Results for reduced Young's moduli for the different samples figure 4.4 suggest that the 1:0.5 compositions have higher reduced Young's modulus ~48 GPa, at indentation depths below 500nm compared to other thin film compositions within the 60 ^{0}C – 80 ^{0}C temperature regimes. Further annealing of samples to 100^{0}C shows significant improvements in the reduced modulus of HTL with 0.3 MoO_3 doping. This composition shows the optimum reduced Young's modulus of about ~72.4G Pa at this temperature regime.

The measured reduced Young's moduli of PEDOT:PSS thin films is between the range of 0.3 GPa and 28.5 GPa for the different heat treatments. Some of these values are relatively high compared to prior measurements of Youngs modulus by Lang et al [89] and Jing Du et al, [90] summarized in table 4.2. These high values can be attributed to the effects of high relative humidity experimental conditions and possible effects of plasticity.

These results also suggest that, the introduction of molybdenum trioxide nanoparticles into the PEDOT:PSS improves its mechanical properties in terms of young's modulus and hardness for all the different heat treatments.

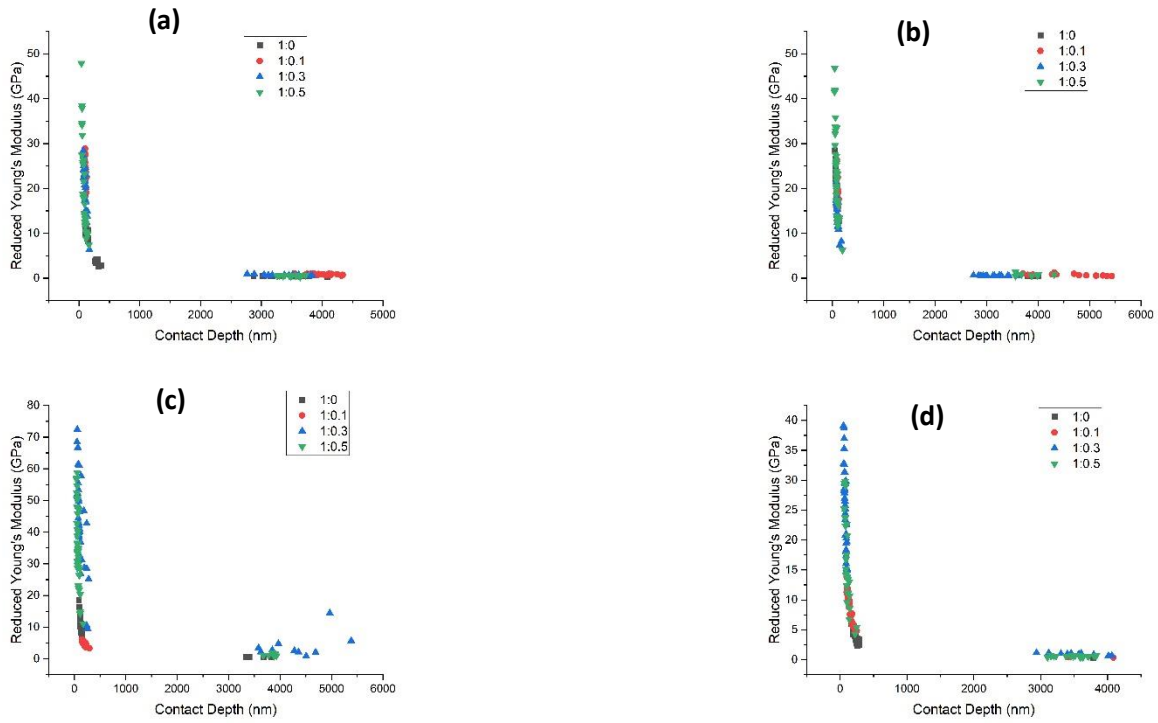

Figure: 4.4: Nanoindentation measurements of Reduced Young's Modulus of PEDOT:PSS and PEDOT:PSS/ammonia-MoO_3 thin film blends [(1:0(ash), 1:0.1(red), 1:0.3(blue), 1:0.5(green)] annealed at a) 60 ^{0}C, b) 80 ^{0}C, c) 100 ^{0}C and d) 120 ^{0}C

Table 4.2: Summary of Young's modulus for PEDOT:PSS and MoO_3 from previous studies and the method of measurement used.

Material	Young's Modulus (GPa)	Method	Reference
PEDOT:PSS	0.3 ~ 28.48	nanoindentation	Current study
	2.26 ± 0.05	Buckling	[91]
	0.9~1.9	Dog-bone tensile test	[92]
	1.42 ±0.07	nanoindentation	[90]
MoO_3	64.6	nanoindentation	[93]

PEDOT:PSS/MoO_3	72.4 GPa	nanoindentation	Current study

4.1.1 Assessment of Load Displacement Curves of Treated Samples

The plots of indentation load against indentation depth for the different thin film compositions and heat treatments in figure 4.5, show the elastic-plastic loading followed by plastic unloading during the nanoindentation process with a maximum load of about 198 μN. There are no visible pop-out or po-in events in the as-prepared PEDOT:PSS and PEDOT:PSS/MoO_3 blend thin films. The results also show that, the hardness and modulus measurements for samples in the 60 ^{0}C and 80 ^{0}C temperature regimes are closely related compared to those that were annealed at 100 ^{0}C and 120 ^{0}C. As earlier mentioned, the thin film blends at lower temperatures showed high crystal growths which disappeared at higher temperatures. These microstructural changes in the samples within the different temperature regimes explains the better correlation in mechanical properties within the lower temperature regimes (60 – 80 ^{0}C). These changes in phases of the samples affected the mechanical properties as shown be fig 4.6c and d.

The Oliver and Pharr method [63] can be used to compute hardness and Young's modulus of samples from the load displacement curves in figure 4.5 a-d.

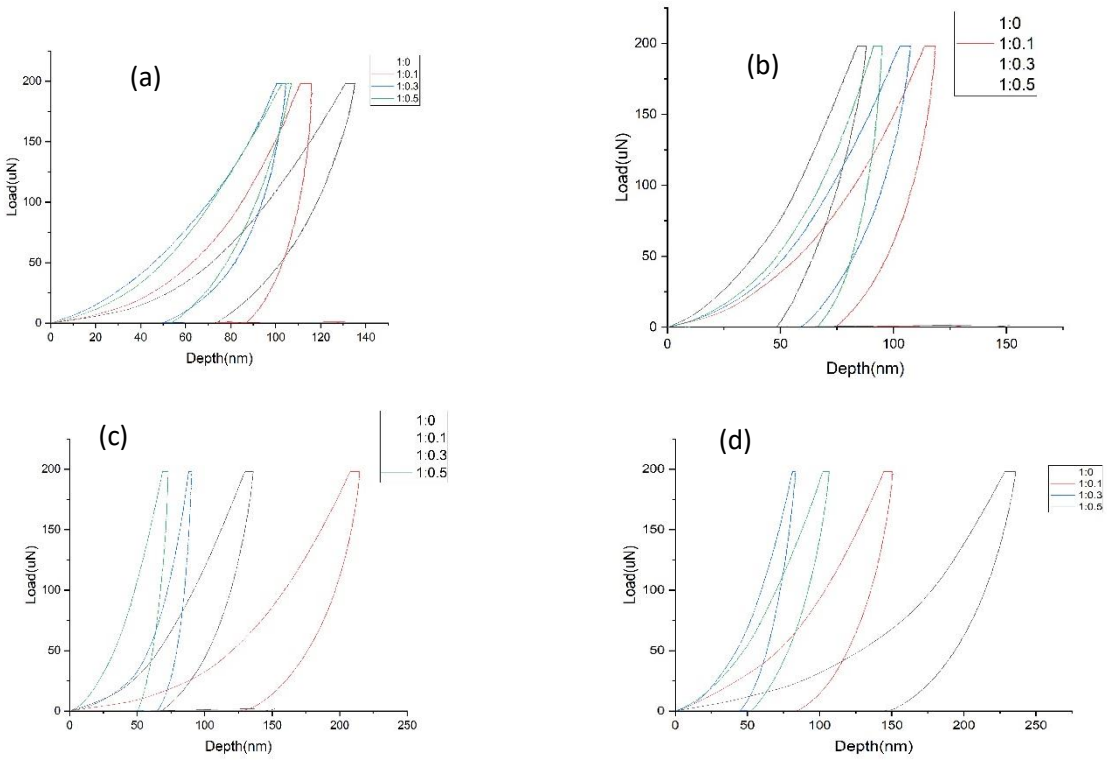

Figure: 4.5: Load displacement curves for PEDOT:PSS and PEDOT:PSS/ammonia-MoO_3 thin film hybrid blends [(1:0(ash), 1:0.1(red), 1:0.3(blue), 1:0.5(green)] annealed at a) 60 ^{0}C, b) 80 ^{0}C, c) 100 ^{0}C and d) 120 ^{0}C

4.4 MAPPING AND STATISTICAL ANALYSIS OF MECHANICAL PROPERTIES

4.4.1 Hardness and Modulus Maps

For further analysis of mechanical properties of the as-prepared samples and thin film blends, mapping of mechanical properties is carried on the raw data of elastic modulus and hardness measured at different contact depths. The procedure for the mechanical mapping and statistical analysis outlined below, was carried out in MATLAB, detailed description of the used code and toolbox is found here [94].

The mechanical maps of experimental data are a representation of the elastic modulus and hardness of the different samples with each pixel representing a nanoindentation test; a linear interpolation of the data by a factor of 4 and smoothing of data are carried out. The linear interpolation step increases numerically, the number of pixels x4 for the maps by using existing data to make predictions thus filling-in missing data, pixelation and noise effects are also minimized leading to a more accurate approximation of the material properties [95], [96]. Large differences between pixel intensity in the mechanical topography as a result of surface effects can lead to sharp peaks or sharp valleys. The smoothing step applied on the raw data aids in reducing these differences in intensity between pixels, and together with the interpolation can be used to improve pixelation, giving rise to cleaner and more readable maps [94].

From the mechanical maps, highest hardness and modulus values are recorded for the MoO_3/PEDOT:PSS composite blend thin films as expected, while lower values are recorded for the as prepared PEDOT:PSS samples as can be observed in figures 4.6a-h and 4.7a-f. According to some prior measurements, reported elastic modulus values of PEDOT:PSS are in the range of 0.8 to 2.8 GPa [92], [97] and 66.8 ± 6.1 GPa for MoO_3 [93].

The presented mechanical maps providing information on the hardness and elastic modulus enables the identification of phases with similar properties. Two predominant phases can be identified in most of the thin film blends where the phases with higher modulus and hardness match with MoO_3 phase, while low values are related to the PEDOT:PSS phases, values for the different phases agree with modulus values from literature [90], [97]. As presented in figure 4.7d, enclosed areas (66.7 and 68.5) represent a common phase and these values corresponds to elastic modulus values for MoO_3 [93].

A mapping of hardness overlay **figure 4.7e** shows that, there were little or no surface effects during the indentation process, the overlay shows minimal errors for the interpolated data after the application of the smoothing step on the raw data.

Also, to easily distinguish between different constituents of the thin films from the mechanical map, a contour plot for elastic modulus corresponding to the interpolated data, is represented in figure 4.8f.

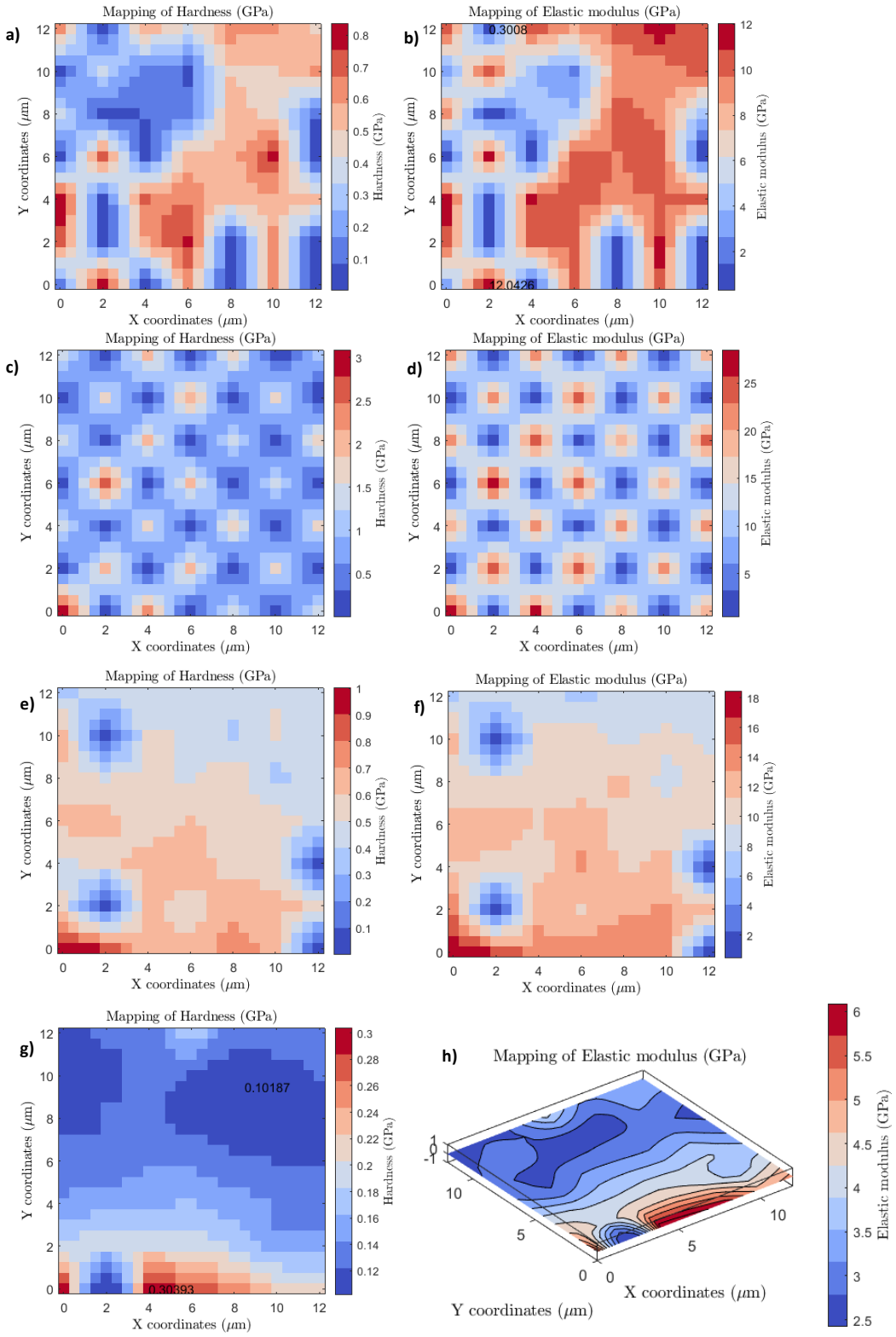
a)
Mapping of Hardness (GPa)
Y coordinates (μm)
X coordinates (μm)
Hardness (GPa)
b)
Mapping of Elastic modulus (GPa)
0.3008
12.0426
Elastic modulus (GPa)
c)
Mapping of Hardness (GPa)
d)
Mapping of Elastic modulus (GPa)
e)
Mapping of Hardness (GPa)
f)
Mapping of Elastic modulus (GPa)
g)
Mapping of Hardness (GPa)
0.10187
0.30393
h)
Mapping of Elastic modulus (GPa)

Figure 4.6: Grid indentation test results for PEDOT:PSS films for different heat treatments (a - d) mapping of hardness at 60 ºC, 80 ºC, 100ºC, and 120 ºC (e-g) mapping of elastic modulus at 60 ºC, 80 ºC, 100 ºC , and 120 ºC respectively (h) contour plot of modulus at 120 ºC

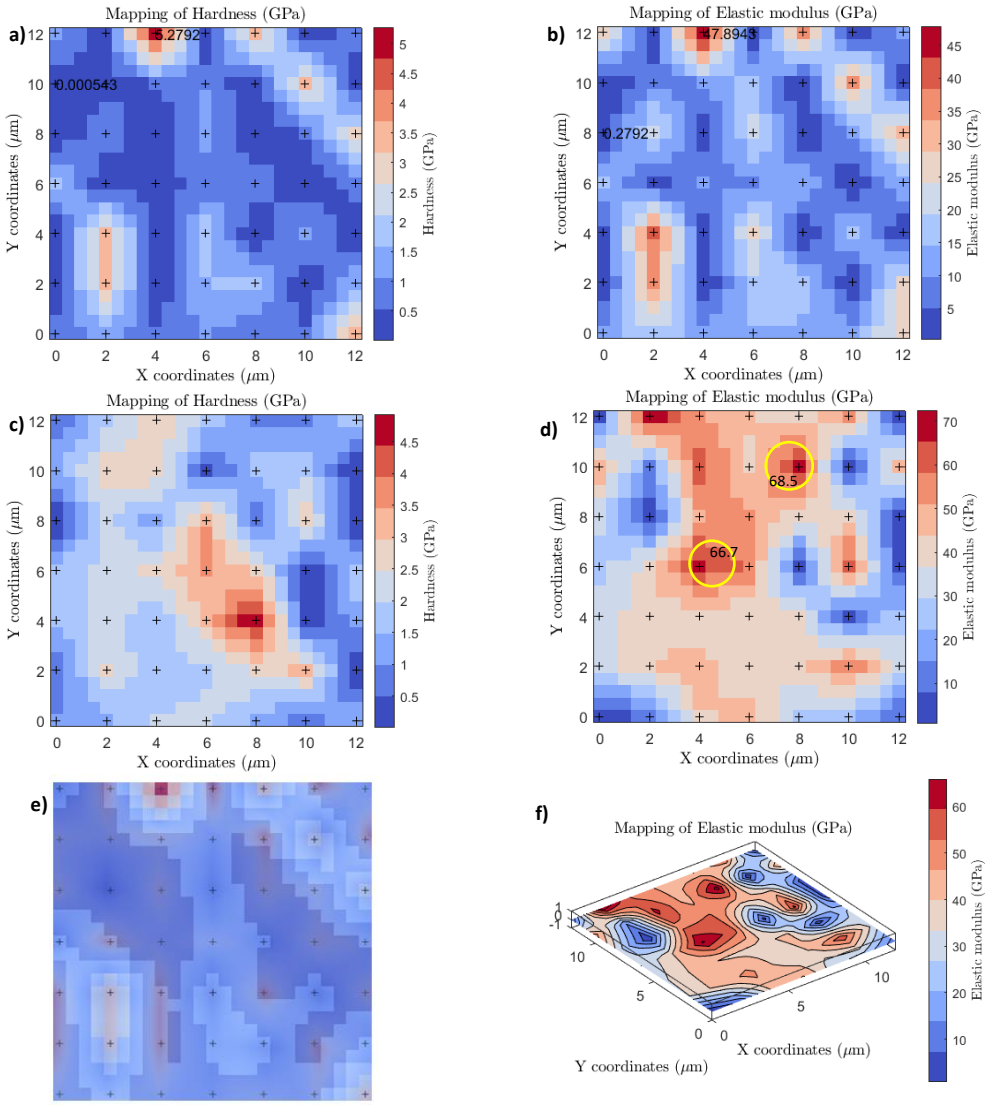

Figure 4.7: Grid indentation test results for MoO_3/PEDOT:PSS thin film blends for different heat treatments (a) mapping of hardness at 60 ºC - 80ºC , 100 ºC, and 120 ºC (b) mapping of elastic modulus at 60 ºC – 80 ºC, (c) mapping of hardness at 100ºC – 120 ºC , (d) mapping of elastic

modulus for 100ºC - 120ºC e) mapping of hardness overlay and (f) contour plot of elastic modulus for 100 ºC – 120 ºC .

4.4.2 Statistical Analysis of Grid Indentation Results.

Histograms representing the elastic modulus and hardness are presented in fig 4.8a corresponding to the grid indentation results on the as prepared PEDOT:PSS thin films and the MoO_3/PEDOT:PSS composite blends. The PDF aids in the visualization of different phases present in the material by identifying different peaks representing these phases.

For a clearer representation of the actual properties of each phase from the peaks, a deconvolution process (gives average values and standard deviations for each peak) was applied to the hardness and modulus results. The setup for the statistical deconvolutions was kept consistent for all statistical data sets, a maximum of four phases were searched at a limiting error for experimental and theoretical density function of $1e^{-6}$. This method helps in the identification of the individual distributions related to each particular phase and the estimation of the volume fractions [98]–[100].

The statistical deconvolution results in figure 4.8a and b show the presence of two predominant phases in the PEDOT:PSS thin film, this is shown by two normal distribution curves after the statistical deconvolution of the indentation data and four phase search. The phases are clearly distinct in the histogram of elastic modulus fig 4.8b.

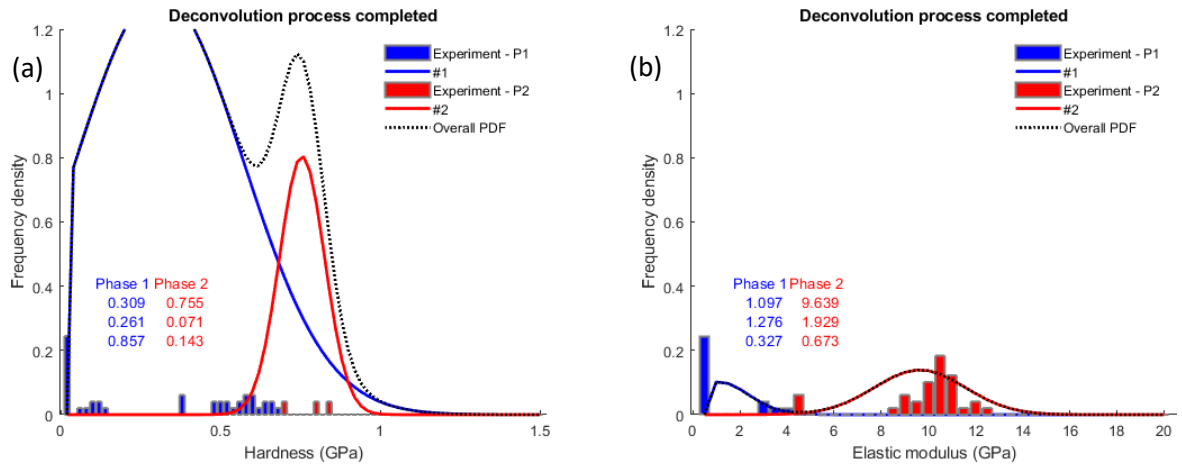

Figure 4.8: Frequency plots of grid indentation results for as prepared PEDOT:PSS annealed at 60C (a) histogram of hardness with deconvolution results for a bin size of 0.02 GPa, (b) histogram of elastic modulus with deconvolution results for a bin size of 0.5 GPa.

Statistical analysis of the thin film blends show the existence of two phases in most cases; the PEDOT:PSS phase and MoO_3 particles with interfaces of PEDOT:PSS and the MoO_3 figures 4.9a-d. However, getting an accurate estimation of the intrinsic properties (elastic modulus) of each of these phases is not so clear since the phases as depicted by the normal distributions are not clearly distinguishable. This is a common problem with grid indentation carried out on composites making it difficult estimate mechanical properties accurately [98]. This difficulty to identify the actual properties of each phase can be associated to difference in the order of magnitude of each phase, effects of interfaces and surrounding phases [101]. Therefore, the phase differentiation was done by nature of the data or order of magnitude of the properties; for example in fig 4.9a higher hardness values corresponds to the MoO_3 nanoparticles likewise, fig 4.9 b and d, higher young's modulus values also correspond to this same nanoparticle. These are obviously approximations of the actual phases since each phase constitutes different components. The bin size also affects the

visualization of the different phases reported, results for fig 4.9a and b are summarized in table 4.3 below.

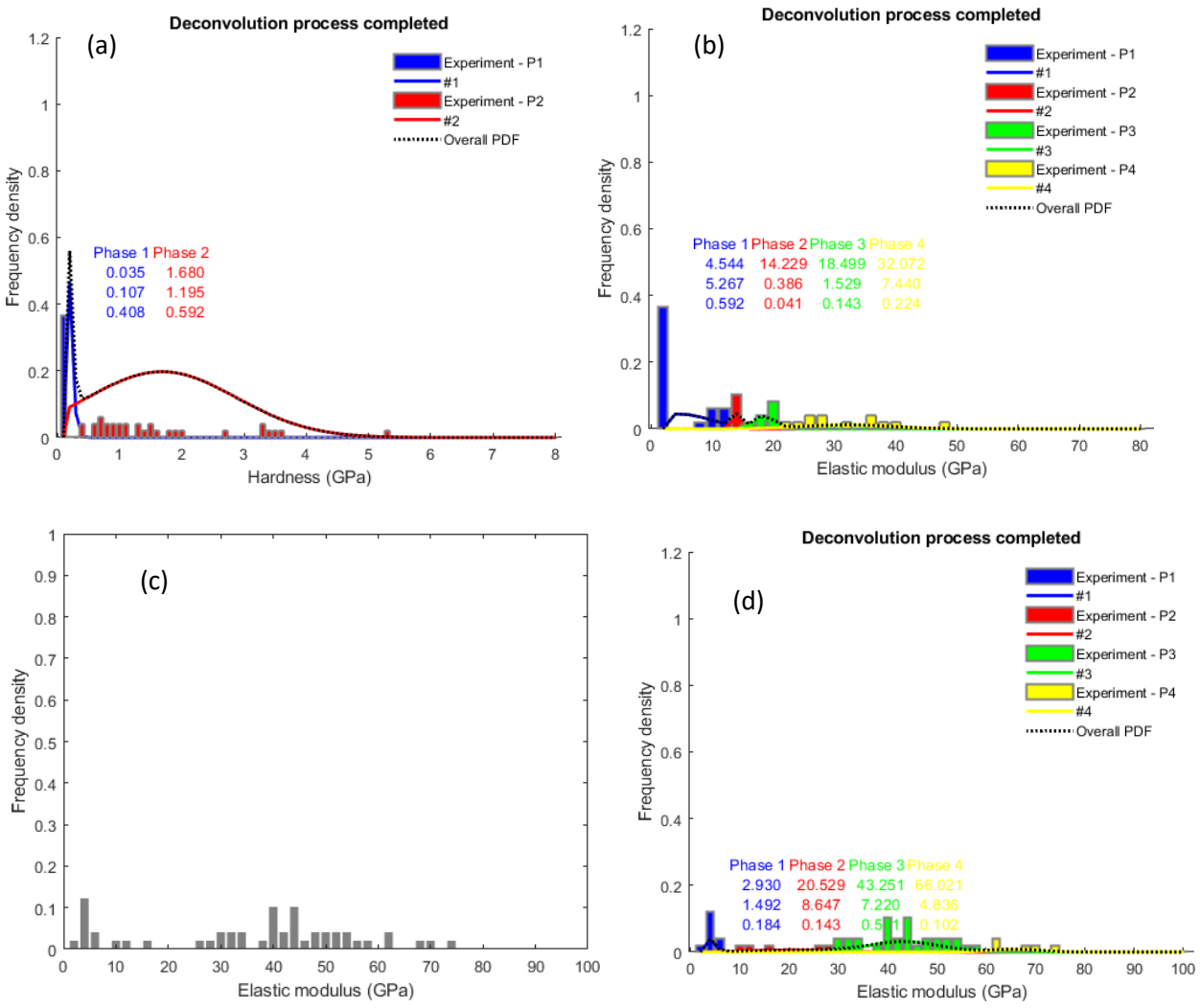

Figure 4.9: Frequency plots of grid indentation results for selected MoO_3/PEDOT:PSS blends (a) histogram of hardness with deconvolution results for a bin size of 0.01 GPa, (b) histogram of elastic modulus with deconvulation results for a bin size of 2 GPa, (c) histogram of elastic modulus, bin size 2 GPa (d) histogram of elastic modulus with deconvolution, bin size 2 GPa.

Table 4.3: Statistical deconvolution results of elastic modulus and hardness for phases present in MoO_3/PEDOT:PSS blends from grid indentation data.

Property	Bin-size	Mechanical property Appearance			
		Phase 1	Phase 2	Phase 3	Phase 4
Hardness	0.01	0.408	1.552	0.02	
	0.02	0.469	1.593	0.02	0.02
	0.1	0.367	1.472	0.02	
Modulus	2	4.864	14.229	18.499	32.072
	5	0.592	0.02	13.897	31.195

4.5 ELECTRICAL SHEET RESISTANCE OF PEDOT:PSS AND PEDOT:PSS/MoO3 ON FTO GLASS

For actual applicability of these thin films as hole transport layers in OPVs or OLEDs, sheet resistance is a major issue which needs to be clarified. In order to understand the effects of blended ratio of MoO3 to PEDOT:PSS on sheet resistance, PEDOT:PSS/MoO_3 hybrid inks are prepared of different blended ratios and annealed at different temperature regimes.

The sheet resistance measurements obtained using a four point probe for the different sample compositions under different annealing temperatures are presented in table 4.4. The results show that samples with 3% MoO_3 have better electrical properties as they possess the lowest sheet resistances between 117 kΩ/sq and 136 kΩ/sq in all the considered temperature regimes. This is closely followed by samples with 1% MoO_3. These results show that just a little percentage (1% – 3%) of the transition metal oxide nanoparticles is needed to improve the electrical properties of PEDOT:PSS for applications as HTL in organic solar cells and organic light emitting diodes.

However, excessive doping with MoO_3 is unfavorable and leads to poor performance, these electrical properties agrees with previous studies by Zhou et al [102]; Excessive dopants such as in samples with 5% dopant show higher electrical sheet resistance which is unfavorable for applications as these, as they can lead to trap states being formed at the different layer interfaces.

Table 4.4: Sheet resistance measurements for pure PEDOT:PSS (CT) and PEDOT:PSS thin fil blends (1:0.1, 1:0.3, 1:0.5) on FTO-glass at different annealing temperatures.

Sample	Blended ratio PEDOT:PSS/MoO_3	Annealing Temperature (^oC)	Sheet Resistance Rs (kΩ/sq)
CT	1:0		163.166
	1:0.1		145.037
	1:0.3	60	135.972
	1:0.5		167.699
CT	1:0		172.231
	1:0.1		126.907
	1:0.3	80	120.109
	1:0.5		163.166
CT	1:0		146.850
	1:0.1		122.375
	1:0.3	100	117.842
	1:0.5		185.828
CT	1:0		151.382
	1:0.1		145.037

	1:0.3	120	133.253
	1:0.5		188.095

These results in table 4.4 also show a general reduction in sheet resistance (Rs) of the thin film blends as annealing temperatures are increased from 60 ^{0}C to 100 ^{0}C. However, there is a sudden increase in sheet resistance within the 120 ^{0}C temperature regime. This sudden increase in sheet resistance of the thin film blends with increase in annealing temperatures can be attributed to the high electrical resistance of the transition metal oxide which builds up as temperatures are increased. Also, blended ratio of MoO_3 and increasing annealing temperatures lead to defects being introduced into the thin film blends as the organic materials are burnout during annealing at higher temperature regimes. The increase in diffusion rates earlier explained can only be possible if there is presence of defects in the thin film blend for vacancy and interstitial diffusion.

CHAPTER FIVE

5.1 CONCLUSION

This work presents the results of the effects of annealing temperatures and MoO_3 doping on the surface morphology, mechanical properties as well as microstructure of solution processed PEDOT:PSS/MoO_3 thin film blends studied for organic photovoltaics and OLED applications. Mechanical maps and statistical convolution showing the distribution of mechanical properties as well as the predominant phases present in these thin film blends are also investigated using TriDiMap in MATLAB.

There is consistency in results obtained from this study with that of other authors, however, much work has not been done on such thin film blends to characterize their mechanical properties. The introduction of the MoO_3 nanoparticles into PEDOT:PSS significantly modifies its microstructure and surface morphology at different annealing temperatures. Also, there are observable microstructural changes in the highly doped thin film blends. Furthermore, the studied mechanical properties; hardness and modulus are significantly improved by the introduction of the transition metal oxide nanoparticles. Furthermore, mechanical maps and statistical deconvolution data for the hardness and elastic modulus for these thin film blends show two predominant phases present in the thin film blends as expected.

From this study, lightly doped thin film blends generally exhibit low sheet resistance, better surface morphologies and better (balance) mechanical properties which are required to develop efficient and mechanical durable electronic devices.

5.2 RECOMMENDATIONS

Further research in this area can focus on investigating the following areas:

Investigate the IV characteristics of the different thin film blend compositions and their corresponding optical transmittances under the different annealing conditions.

Also, the effects of defects on sheet resistance can be further investigated for the various thin film blends to understand how the sheets resistance can be maintained at a minimum to achieve optimal device performance. Finally, an actual device should be fabricated using the thin film blend with an optimum balance of properties necessary for an efficient and durable device.

5.3 REFERENCES

[1] R. Wang, M. Mujahid, Y. Duan, Z.-K. Wang, J. Xue, and Y. Yang, "A Review of Perovskites Solar Cell Stability," *Adv. Funct. Mater.*, vol. 29, no. 47, p. 1808843, 2019, doi: 10.1002/adfm.201808843.

[2] A. Jäger-Waldau, "Photovoltaics: Status and Perspectives until 2020," *Green - Int. J. Sustain. Energy Convers. Storage*, vol. 1, pp. 277–290, Nov. 2011, doi: 10.1515/green.2011.027.

[3] U. Nations, "Generating power," *United Nations*. https://www.un.org/en/climatechange/climate-solutions/cities-pollution (accessed Jul. 14, 2022).

[4] N. Sun, C. Jiang, Q. Li, D. Tan, S. Bi, and J. Song, "Performance of OLED under mechanical strain: a review," *J. Mater. Sci. Mater. Electron.*, vol. 31, no. 23, Art. no. 23, Dec. 2020, doi: 10.1007/s10854-020-04652-5.

[5] X. Dai, K. Xu, and F. Wei, "Recent progress in perovskite solar cells: the perovskite layer," *Beilstein J. Nanotechnol.*, vol. 11, pp. 51–60, Jan. 2020, doi: 10.3762/bjnano.11.5.

[6] J. J. Yoo *et al.*, "Efficient perovskite solar cells via improved carrier management," *Nature*, vol. 590, no. 7847, pp. 587–593, Feb. 2021, doi: 10.1038/s41586-021-03285-w.

[7] "Perovskite Solar Cells - an overview | ScienceDirect Topics," Aug. 29, 2021. https://www.sciencedirect.com/topics/engineering/perovskite-solar-cells (accessed Aug. 29, 2021).

[8] K. Valadi, S. Gharibi, R. Taheri-Ledari, S. Akin, A. Maleki, and A. Shalan, “Metal oxide electron transport materials for perovskite solar cells: a review,” *Environ. Chem. Lett.*, vol. 19, Jan. 2021, doi: 10.1007/s10311-020-01171-x.

[9] M. Khan *et al.*, “Experimental and Numerical Analysis of Nanoindentation of Ti-6246 Alloy,” *Part. Sci. Technol.*, vol. 36, Jan. 2017, doi: 10.1080/02726351.2016.1267287.

[10] J. Dean, A. Bradbury, G. Aldrich-Smith, and T. W. Clyne, “A procedure for extracting primary and secondary creep parameters from nanoindentation data,” *Mech. Mater.*, vol. 65, pp. 124–134, Oct. 2013, doi: 10.1016/j.mechmat.2013.05.014.

[11] “Yield Strength Testing - [PDF Document].” https://cupdf.com/document/yield-strength-testing.html (accessed Jul. 19, 2022).

[12] R. Iankov, M. Datcheva, S. Cherneva, and D. Stoychev, “Finite Element Simulation of Nanoindentation Process,” in *Numerical Analysis and Its Applications*, I. Dimov, I. Faragó, and L. Vulkov, Eds., in Lecture Notes in Computer Science, vol. 8236. Berlin, Heidelberg: Springer Berlin Heidelberg, 2013, pp. 319–326. doi: 10.1007/978-3-642-41515-9_35.

[13] G. Bolzon, V. Buljak, G. Maier, and B. Miller, “Assessment of elastic–plastic material parameters comparatively by three procedures based on indentation test and inverse analysis,” *Inverse Probl. Sci. Eng.*, vol. 19, no. 6, pp. 815–837, Sep. 2011, doi: 10.1080/17415977.2011.551931.

[14] S. Li, Y.-L. Cao, W.-H. Li, and Z.-S. Bo, “A brief review of hole transporting materials commonly used in perovskite solar cells,” *Rare Met.*, vol. 40, no. 10, pp. 2712–2729, Oct. 2021, doi: 10.1007/s12598-020-01691-z.

[15] M. A. Green, “Photovoltaic principles,” *Phys. E Low-Dimens. Syst. Nanostructures*, vol. 14, no. 1, pp. 11–17, Apr. 2002, doi: 10.1016/S1386-9477(02)00354-5.

[16] D. M. Chapin, C. S. Fuller, and G. L. Pearson, “A New Silicon *p-n* Junction Photocell for Converting Solar Radiation into Electrical Power,” *J. Appl. Phys.*, vol. 25, no. 5, pp. 676–677, May 1954, doi: 10.1063/1.1721711.

[17] A. Le Donne, A. Scaccabarozzi, S. Tombolato, M. Acciarri, A. Abbotto, and S. Binetti, “Solar Photovoltaics: A Review,” *Rev. Adv. Sci. Eng.*, vol. 2, pp. 170–178, May 2013, doi: 10.1166/rase.2013.1030.

[18] E. Katz, “Perovskite: Name Puzzle and German-Russian Odyssey of Discovery,” *Helv. Chim. Acta*, vol. 103, Apr. 2020, doi: 10.1002/hlca.202000061.

[19] A. Husainat, W. Ali, P. Cofie, J. Attia, and J. Fuller, “Simulation and Analysis of Methylammonium Lead Iodide ($CH_3NH_3PbI_3$) Perovskite Solar Cell with Au Contact Using SCAPS 1D Simulator,” *Am. J. Opt. Photonics*, vol. 7, no. 2, Art. no. 2, Aug. 2019, doi: 10.11648/j.ajop.20190702.12.

[20] A. B. Coulibaly, S. O. Oyedele, N. R. Kre, and B. Aka, “Comparative Study of Lead-Free Perovskite Solar Cells Using Different Hole Transporter Materials,” *Model. Numer. Simul. Mater. Sci.*, vol. 9, no. 4, Art. no. 4, Sep. 2019, doi: 10.4236/mnsms.2019.94006.

[21] S. Sun *et al.*, “The origin of high efficiency in low-temperature solution-processable bilayer organometal halide hybrid solar cells,” *Energy Env. Sci*, vol. 7, no. 1, pp. 399–407, 2014, doi: 10.1039/C3EE43161D.

[22] C. C. Stoumpos, C. D. Malliakas, and M. G. Kanatzidis, “Semiconducting Tin and Lead Iodide Perovskites with Organic Cations: Phase Transitions, High Mobilities, and Near-Infrared Photoluminescent Properties,” *Inorg. Chem.*, vol. 52, no. 15, pp. 9019–9038, Aug. 2013, doi: 10.1021/ic401215x.

[23] D. Zhou, T. Zhou, Y. Tian, X. Zhu, and Y. Tu, “Perovskite-Based Solar Cells: Materials, Methods, and Future Perspectives,” *J. Nanomater.*, vol. 2018, p. e8148072, Jan. 2018, doi: 10.1155/2018/8148072.

[24] M. Era, S. Morimoto, T. Tsutsui, and S. Saito, “Organic-inorganic heterostructure electroluminescent device using a layered perovskite semiconductor (C6H5C2H4NH3)2PbI4,” *Appl. Phys. Lett.*, vol. 65, no. 6, pp. 676–678, Aug. 1994, doi: 10.1063/1.112265.

[25] I. Koutselas, P. Bampoulis, E. Maratou, T. Evagelinou, G. Pagona, and G. Papavassiliou, “Some Unconventional Organic−Inorganic Hybrid Low-Dimensional Semiconductors and Related Light-Emitting Devices,” *J. Phys. Chem. C*, vol. 115, Apr. 2011, doi: 10.1021/jp111881b.

[26] Y. Cao *et al.*, “Perovskite light-emitting diodes based on spontaneously formed submicrometre-scale structures,” *Nature*, vol. 562, no. 7726, Art. no. 7726, Oct. 2018, doi: 10.1038/s41586-018-0576-2.

[27] H. Cho *et al.*, “Overcoming the electroluminescence efficiency limitations of perovskite light-emitting diodes,” *Science*, vol. 350, no. 6265, pp. 1222–1225, Dec. 2015, doi: 10.1126/science.aad1818.

[28] Y.-H. Kim *et al.*, “Multicolored Organic/Inorganic Hybrid Perovskite Light-Emitting Diodes,” *Adv. Mater.*, vol. 27, no. 7, pp. 1248–1254, 2015, doi: 10.1002/adma.201403751.

[29] K. Lin *et al.*, "Perovskite light-emitting diodes with external quantum efficiency exceeding 20 per cent," *Nature*, vol. 562, no. 7726, Art. no. 7726, Oct. 2018, doi: 10.1038/s41586-018-0575-3.

[30] Z.-K. Tan *et al.*, "Bright light-emitting diodes based on organometal halide perovskite," *Nat. Nanotechnol.*, vol. 9, no. 9, Art. no. 9, Sep. 2014, doi: 10.1038/nnano.2014.149.

[31] A. Bonadio *et al.*, "Entropy-driven stabilization of the cubic phase of $MaPbI_3$ at room temperature," *J. Mater. Chem. A*, vol. 9, no. 2, pp. 1089–1099, 2021, doi: 10.1039/D0TA10492B.

[32] F. Lehmann *et al.*, "The phase diagram of a mixed halide (Br, I) hybrid perovskite obtained by synchrotron X-ray diffraction," *RSC Adv.*, vol. 9, no. 20, pp. 11151–11159, 2019, doi: 10.1039/C8RA09398A.

[33] Z. Shi and A. Jayatissa, "Perovskites-Based Solar Cells: A Review of Recent Progress, Materials and Processing Methods," *Materials*, vol. 11, May 2018, doi: 10.3390/ma11050729.

[34] B. Osman, T. Abdolkader, and I. Sayed Ahmed, "A Review of Perovskite Solar Cells," *Int. J. Mater. Technol. Innov.*, vol. 1, pp. 48–66, Nov. 2021, doi: 10.21608/ijmti.2021.78369.1032.

[35] A. Merad, M. Kanoun, and K. Ahmed-Ali, "Toward development of high-performance perovskite solar cells based on CH3NH3GeI3 using computational approach," *Sol. Energy*, vol. 182, pp. 237–244, Apr. 2019, doi: 10.1016/j.solener.2019.02.041.

[36] J. C. Bernède, "ORGANIC PHOTOVOLTAIC CELLS: HISTORY, PRINCIPLE AND TECHNIQUES," *J. Chil. Chem. Soc.*, vol. 53, no. 3, Sep. 2008, doi: 10.4067/S0717-97072008000300001.

[37] Y. Wu, D. Wang, J. Liu, and H. Cai, "Review of Interface Passivation of Perovskite Layer," *Nanomaterials*, vol. 11, no. 3, Art. no. 3, Mar. 2021, doi: 10.3390/nano11030775.

[38] Z. Zhu *et al.*, "Mesoporous SnO2 Single Crystals as an Effective Electron Collector for Perovskite Solar Cells," *Phys Chem Chem Phys*, vol. 17, Jun. 2015, doi: 10.1039/C5CP01534K.

[39] Z. Song, S. Watthage, A. Phillips, and M. Heben, "Pathways toward high-performance perovskite solar cells: Review of recent advances in organo-metal halide perovskites for photovoltaic applications," *J. Photonics Energy*, vol. 6, p. 022001, Apr. 2016, doi: 10.1117/1.JPE.6.022001.

[40] G. Niu, X. Guo, and L. Wang, "Review of recent progress in chemical stability of perovskite solar cells," *J. Mater. Chem. A*, vol. 3, no. 17, pp. 8970–8980, 2015, doi: 10.1039/C4TA04994B.

[41] G. Kieslich, S. Sun, and A. K. Cheetham, "Solid-state principles applied to organic–inorganic perovskites: new tricks for an old dog," *Chem. Sci.*, vol. 5, no. 12, pp. 4712–4715, Oct. 2014, doi: 10.1039/C4SC02211D.

[42] A. Amat *et al.*, "Cation-Induced Band-Gap Tuning in Organohalide Perovskites: Interplay of Spin–Orbit Coupling and Octahedra Tilting," *Nano Lett.*, vol. 14, no. 6, pp. 3608–3616, Jun. 2014, doi: 10.1021/nl5012992.

[43] G. Niu, W. Li, F. Meng, L. Wang, H. Dong, and Y. Qiu, “Study on the stability of CH3NH3PbI3 films and the effect of post-modification by aluminum oxide in all-solid-state hybrid solar cells,” *J. Mater. Chem. A*, vol. 2, no. 3, pp. 705–710, Dec. 2013, doi: 10.1039/C3TA13606J.

[44] H. Zhou *et al.*, “Interface engineering of highly efficient perovskite solar cells,” *Science*, vol. 345, no. 6196, pp. 542–546, Aug. 2014, doi: 10.1126/science.1254050.

[45] P. Van De Weijer, P. C. P. Bouten, S. Unnikrishnan, H. B. Akkerman, J. J. Michels, and T. M. B. Van Mol, “High-performance thin-film encapsulation for organic light-emitting diodes,” *Org. Electron.*, vol. 44, pp. 94–98, May 2017, doi: 10.1016/j.orgel.2017.02.009.

[46] N. Chander *et al.*, “Reduced ultraviolet light induced degradation and enhanced light harvesting using YVO4:Eu3+ down-shifting nano-phosphor layer in organometal halide perovskite solar cells,” *Appl. Phys. Lett.*, vol. 105, no. 3, p. 033904, Jul. 2014, doi: 10.1063/1.4891181.

[47] Y.-H. Kim, S.-H. Lee, J. Noh, and S.-H. Han, “Performance and stability of electroluminescent device with self-assembled layers of poly(3,4-ethylenedioxythiophene)–poly(styrenesulfonate) and polyelectrolytes,” *Thin Solid Films*, vol. 510, no. 1, pp. 305–310, Jul. 2006, doi: 10.1016/j.tsf.2005.08.174.

[48] J.-S. Kim, R. H. Friend, I. Grizzi, and J. H. Burroughes, “Spin-cast thin semiconducting polymer interlayer for improving device efficiency of polymer light-emitting diodes,” *Appl. Phys. Lett.*, vol. 87, no. 2, p. 023506, Jul. 2005, doi: 10.1063/1.1992658.

[49] V. Shrotriya, G. Li, Y. Yao, C.-W. Chu, and Y. Yang, “Transition metal oxides as the buffer layer for polymer photovoltaic cells,” *Appl. Phys. Lett.*, vol. 88, no. 7, p. 073508, Feb. 2006, doi: 10.1063/1.2174093.

[50] W. Shi, N. Liu, Y. Zhou, and X. Cao, “Effects of Postannealing on the Characteristics and Reliability of Polyfluorene Organic Light-Emitting Diodes,” *IEEE Trans. Electron Devices*, vol. PP, pp. 1–6, Jan. 2019, doi: 10.1109/TED.2018.2888858.

[51] Y. Zhao, J. Chen, W. Chen, and D. Ma, “Poly(3,4-ethylenedioxythiophene):poly(styrenesulfonate)/MoO3 composite layer for efficient and stable hole injection in organic semiconductors,” *J. Appl. Phys.*, vol. 111, no. 4, p. 043716, Feb. 2012, doi: 10.1063/1.3687933.

[52] J.-Y. Sun *et al.*, “Performance enhancement in inverted polymer photovoltaics with solution-processed MoOX and air-plasma treatment for anode modification,” *Sol. Energy Mater. Sol. Cells*, vol. 109, pp. 178–184, Feb. 2013, doi: 10.1016/j.solmat.2012.10.026.

[53] S. Murase and Y. Yang, “Solution Processed MoO3 Interfacial Layer for Organic Photovoltaics Prepared by a Facile Synthesis Method,” *Adv. Mater.*, vol. 24, no. 18, pp. 2459–2462, 2012, doi: 10.1002/adma.201104771.

[54] F. Hou *et al.*, “Efficient and stable planar heterojunction perovskite solar cells with an MoO3/PEDOT:PSS hole transporting layer,” *Nanoscale*, vol. 7, no. 21, pp. 9427–9432, May 2015, doi: 10.1039/C5NR01864A.

[55] H. Sung *et al.*, “Transparent Conductive Oxide-Free Graphene-Based Perovskite Solar Cells with over 17% Efficiency,” *Adv. Energy Mater.*, vol. 6, no. 3, p. 1501873, 2016, doi: 10.1002/aenm.201501873.

[56] Q. Zheng *et al.*, "Solution-Processed Composite Interfacial Layer of MoOx-Doped Graphene Oxide for Robust Hole Injection in Organic Light-Emitting Diode," *Phys. Status Solidi RRL – Rapid Res. Lett.*, vol. 12, no. 4, p. 1700434, 2018, doi: 10.1002/pssr.201700434.

[57] D. B. Kim *et al.*, "Improved performance of perovskite light-emitting diodes using a PEDOT:PSS and MoO3 composite layer," *J. Mater. Chem. C*, vol. 4, no. 35, pp. 8161–8165, Sep. 2016, doi: 10.1039/C6TC02099B.

[58] Y. Meng *et al.*, "High performance and stable all-inorganic perovskite light emitting diodes by reducing luminescence quenching at PEDOT:PSS/Perovskites interface," *Org. Electron.*, vol. 64, pp. 47–53, Jan. 2019, doi: 10.1016/j.orgel.2018.10.014.

[59] J. M. Wheeler and J. Michler, "Invited Article: Indenter materials for high temperature nanoindentation," *Rev. Sci. Instrum.*, vol. 84, no. 10, p. 101301, Oct. 2013, doi: 10.1063/1.4824710.

[60] D. M. Ebenstein and L. A. Pruitt, "Nanoindentation of biological materials," *Nano Today*, vol. 1, no. 3, pp. 26–33, Aug. 2006, doi: 10.1016/S1748-0132(06)70077-9.

[61] Z. Hu, K. Lynne, and F. Delfanian, "Characterization of materials' elasticity and yield strength through micro-/nano-indentation testing with a cylindrical flat-tip indenter," *J. Mater. Res.*, vol. 30, no. 4, pp. 578–591, Feb. 2015, doi: 10.1557/jmr.2015.4.

[62] A. S. Alaboodi and Z. Hussain, "Finite element modeling of nano-indentation technique to characterize thin film coatings," *J. King Saud Univ. - Eng. Sci.*, vol. 31, no. 1, pp. 61–69, Jan. 2019, doi: 10.1016/j.jksues.2017.02.001.

[63] W. C. Oliver and G. M. Pharr, “An improved technique for determining hardness and elastic modulus using load and displacement sensing indentation experiments,” *J. Mater. Res.*, vol. 7, no. 6, pp. 1564–1583, Jun. 1992, doi: 10.1557/JMR.1992.1564.

[64] D. A. Lucca, K. Herrmann, and M. J. Klopfstein, “Nanoindentation: Measuring methods and applications,” *CIRP Ann.*, vol. 59, no. 2, pp. 803–819, 2010, doi: 10.1016/j.cirp.2010.05.009.

[65] J. Tomastik and R. Ctvrtlik, “Nanoscratch test — A tool for evaluation of cohesive and adhesive properties of thin films and coatings,” *EPJ Web Conf.*, vol. 48, p. 00027, Apr. 2013, doi: 10.1051/epjconf/20134800027.

[66] N. Randall, G. Favaro, and C. Frankel, “The Effect of Intrinsic Parameters on the Critical Load as Measured With the Scratch Test Method,” *Surf. Coat. Technol. - SURF COAT TECH*, vol. 137, pp. 146–151, Mar. 2001, doi: 10.1016/S0257-8972(00)01097-5.

[67] G. Subhash and W. Zhang, “Investigation of the Overall Friction Coefficient in Single-Pass Scratch Test,” *Wear*, vol. 252, pp. 123–134, Jan. 2002, doi: 10.1016/S0043-1648(01)00852-3.

[68] S. H. Im, J. H. Heo, H. Han, D. Kim, and T. Ahn, “18.1% Hysteresis-Less Inverted CH3NH3PbI3 Planar Perovskite Hybrid Solar Cells,” *Energy Env. Sci*, vol. 8, Apr. 2015, doi: 10.1039/C5EE00120J.

[69] T. Y. Tsui and G. M. Pharr, “Substrate effects on nanoindentation mechanical property measurement of soft films on hard substrates,” *J. Mater. Res.*, vol. 14, no. 1, pp. 292–301, Jan. 1999, doi: 10.1557/JMR.1999.0042.

[70] T. Ohmura, S. Matsuoka, K. Tanaka, and T. Yoshida, “Nanoindentation load–displacement behavior of pure face centered cubic metal thin films on a hard substrate,” *Thin Solid Films*, vol. 385, no. 1–2, pp. 198–204, Apr. 2001, doi: 10.1016/S0040-6090(00)01907-6.

[71] R. Saha and W. D. Nix, “Soft films on hard substrates — nanoindentation of tungsten films on sapphire substrates,” *Mater. Sci. Eng. A*, vol. 319–321, pp. 898–901, Dec. 2001, doi: 10.1016/S0921-5093(01)01076-0.

[72] G. Alcalá, P. Skeldon, G. E. Thompson, A. B. Mann, H. Habazaki, and K. Shimizu, “Mechanical properties of amorphous anodic alumina and tantala films using nanoindentation,” *Nanotechnology*, vol. 13, no. 4, pp. 451–455, Aug. 2002, doi: 10.1088/0957-4484/13/4/302.

[73] S. J. Bull, “Modelling of the mechanical and tribological properties of coatings and surface treatments,” *MRS Proc.*, vol. 750, p. Y6.1, 2002, doi: 10.1557/PROC-750-Y6.1.

[74] B. Bhushan and X. Li, “Nanomechanical characterisation of solid surfaces and thin films,” *Int. Mater. Rev.*, vol. 48, no. 3, pp. 125–164, Jun. 2003, doi: 10.1179/095066003225010227.

[75] Z. Shan and S. K. Sitaraman, “Elastic–plastic characterization of thin films using nanoindentation technique,” *Thin Solid Films*, vol. 437, no. 1, pp. 176–181, Aug. 2003, doi: 10.1016/S0040-6090(03)00663-1.

[76] T.-H. Fang, S.-R. Jian, and D.-S. Chuu, “Nanomechanical properties of TiC, TiN and TiCN thin films using scanning probe microscopy and nanoindentation,” *Appl. Surf. Sci.*, vol. 228, no. 1–4, pp. 365–372, Apr. 2004, doi: 10.1016/j.apsusc.2004.01.053.

[77] Z. Xia *et al.*, Eds., "Mechanical properties of highly ordered nanoporous anodic alumina membranes," *Rev. Adv. Mater. Sci.*, 2004.

[78] J. Bressan, A. Tramontin, and C. Rosa, "Modeling of nanoindentation of bulk and thin film by finite element method," *Wear*, vol. 258, pp. 115–122, Jan. 2005, doi: 10.1016/j.wear.2004.05.021.

[79] W. Ni and Y.-T. Cheng, "Modeling conical indentation in homogeneous materials and in hard films on soft substrates," *J. Mater. Res.*, vol. 20, no. 2, pp. 521–528, Feb. 2005, doi: 10.1557/JMR.2005.0071.

[80] X. Huang, "Mechanical characterization of thin film materials with nanoindentation measurement and finite element analysis," Jan. 2005.

[81] X. Huang and A. A. Pelegri, "Mechanical Characterization of Thin Film Materials with Nanoindentation Measurements and FE Analysis," *J. Compos. Mater.*, vol. 40, no. 15, pp. 1393–1407, Aug. 2006, doi: 10.1177/0021998305059728.

[82] M. Zhao, Y. Xiang, J. Xu, N. Ogasawara, N. Chiba, and X. Chen, "Determining mechanical properties of thin films from the loading curve of nanoindentation testing," *Thin Solid Films*, vol. 516, no. 21, pp. 7571–7580, Sep. 2008, doi: 10.1016/j.tsf.2008.03.018.

[83] H. Li and J. Vlassak, "Determining the Elastic Modulus and Hardness of an Ultrathin Film on a Substrate Using Nanoindentation," *J. Mater. Res.*, vol. 24, pp. 1114–1126, Mar. 2009, doi: 10.1557/jmr.2009.0144.

[84] M. Cabibbo, D. Ciccarelli, and S. Spigarelli, “Nanoindentation Hardness Measurement in Piling up SiO2 Coating,” *Phys. Procedia*, vol. 40, pp. 100–112, Jan. 2013, doi: 10.1016/j.phpro.2012.12.014.

[85] W. Zhang, “Mechanical characterization of YBCO thin films using nanoindentation and finite element method,” *Int. J. Mater. Res.*, vol. 108, no. 9, pp. 732–740, Sep. 2017, doi: 10.3139/146.111533.

[86] M. ElMahmoudy, S. Inal, A. Charrier, I. Uguz, G. G. Malliaras, and S. Sanaur, “Tailoring the Electrochemical and Mechanical Properties of PEDOT:PSS Films for Bioelectronics,” *Macromol. Mater. Eng.*, vol. 302, no. 5, p. 1600497, May 2017, doi: 10.1002/mame.201600497.

[87] W. Zhang *et al.*, “Experimental Study on the Thickness-Dependent Hardness of SiO2 Thin Films Using Nanoindentation,” *Coatings*, vol. 11, no. 1, p. 23, Dec. 2020, doi: 10.3390/coatings11010023.

[88] Sura. K. Jebur, A. Braihi, and A. Hassan, “Graphene effects on the structural, morphological and optical properties of PEDOT:PSS thin films,” *Mater. Today Proc.*, vol. 49, Oct. 2021, doi: 10.1016/j.matpr.2021.09.255.

[89] U. Lang, N. Naujoks, and J. Dual, “Mechanical characterization of PEDOT:PSS thin films,” *Synth. Met.*, vol. 159, no. 5–6, pp. 473–479, Mar. 2009, doi: 10.1016/j.synthmet.2008.11.005.

[90] Jing Du, T. Tong, W. Akande, A. Tsakiridou, and W. Soboyejo, “Pressure Effects on the Lamination of Organic Light-Emitting Diodes,” *J. Disp. Technol.*, vol. 9, no. 8, pp. 601–606, Aug. 2013, doi: 10.1109/JDT.2013.2253085.

[91] D. Tahk, H. H. Lee, and D.-Y. Khang, “Elastic Moduli of Organic Electronic Materials by the Buckling Method,” *Macromolecules*, vol. 42, no. 18, pp. 7079–7083, Sep. 2009, doi: 10.1021/ma900137k.

[92] U. Lang, N. Naujoks, and J. Dual, “Mechanical characterization of PEDOT:PSS thin films,” *Synth. Met.*, vol. 159, pp. 473–479, Mar. 2009, doi: 10.1016/j.synthmet.2008.11.005.

[93] J. Du, V. C. Anye, E. O. Vodah, T. Tong, M. Zebaze Kana, and W. Soboyejo, “Pressure-assisted fabrication of organic light emitting diodes with MoO3 hole-injection layer materials,” *J. Appl. Phys.*, vol. 115, pp. 233703–233703, Jun. 2014, doi: 10.1063/1.4881780.

[94] D. Mercier, *TriDiMap Toolbox documentation*. 2018. doi: 10.13140/RG.2.2.25088.89600.

[95] D. Mercier, J.-F. Vanhumbeeck, M. Caruso, and X. V. Eyndes, “Caractérisation mécanique par nanoindentation d’un revêtement composite à matrice nickel électrodéposé,” *Matér. Tech.*, vol. 105, no. 1, Art. no. 1, 2017, doi: 10.1051/mattech/2017014.

[96] D. Mercier, J.-F. Vanhumbeeck, M. Caruso, X. Vanden Eynde, and M. Febvre, “Microstructural and mechanical characterization of electroplated nickel matrix composite coatings,” *Surf. Eng.*, vol. 0, pp. 1–12, Apr. 2018, doi: 10.1080/02670844.2018.1433270.

[97] J. Qu, L. Ouyang, C. Kuo, and D. C. Martin, “Stiffness, strength and adhesion characterization of electrochemically deposited conjugated polymer films,” *Acta Biomater.*, vol. 31, pp. 114–121, Feb. 2016, doi: 10.1016/j.actbio.2015.11.018.

[98] G. Constantinides, K. S. Ravi Chandran, F.-J. Ulm, and K. J. Van Vliet, "Grid indentation analysis of composite microstructure and mechanics: Principles and validation," *Mater. Sci. Eng. A*, vol. 430, no. 1–2, pp. 189–202, Aug. 2006, doi: 10.1016/j.msea.2006.05.125.

[99] J. Nemecek, "Nanoindentation Based Analysis of Heterogeneous Structural Materials," in *Nanoindentation in Materials Science*, J. Nemecek, Ed., InTech, 2012. doi: 10.5772/50968.

[100] V. Hrbek and V. Koudelková, "Grid Indentation and Statistic Deconvolution: Limitations and Accuracy," *Key Eng. Mater.*, vol. 731, pp. 15–22, Mar. 2017, doi: 10.4028/www.scientific.net/KEM.731.15.

[101] S. Kossman *et al.*, "Mechanical characterization by multiscale instrumented indentation of highly heterogeneous materials for braking applications," *J. Mater. Sci.*, vol. 54, no. 6, pp. 4647–4670, Mar. 2019, doi: 10.1007/s10853-018-3158-7.

[102] Y. Zhou *et al.*, "Improved Efficiency of Perovskite Light-Emitting Diodes Using a Three-Step Spin-Coated CH3NH3PbBr3 Emitter and a PEDOT:PSS/MoO3-Ammonia Composite Hole Transport Layer," *Micromachines*, vol. 10, no. 7, p. 459, Jul. 2019, doi: 10.3390/mi10070459.